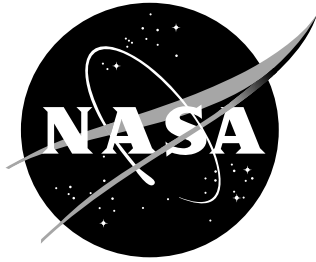


NASA/CR-2000-210102



# Implementation of Advanced Two Equation Turbulence Models in the USM3D Unstructured Flow Solver

*Qunzhen Wang, Steven J. Massey, and Khaled S. Abdol-Hamid*  
*Analytical Services & Materials Inc., Lancaster, CA*

---

April 2000

## The NASA STI Program Office ... in Profile

Since its founding, NASA has been dedicated to the advancement of aeronautics and space science. The NASA Scientific and Technical Information (STI) Program Office plays a key part in helping NASA maintain this important role.

The NASA STI Program Office is operated by Langley Research Center, the lead center for NASA's scientific and technical information. The NASA STI Program Office provides access to the NASA STI Database, the largest collection of aeronautical and space science STI in the world. The Program Office is also NASA's institutional mechanism for disseminating the results of its research and development activities. These results are published by NASA in the NASA STI Report Series, which includes the following report types:

- **TECHNICAL PUBLICATION.** Reports of completed research or a major significant phase of research that present the results of NASA programs and include extensive data or theoretical analysis. Includes compilations of significant scientific and technical data and information deemed to be of continuing reference value. NASA counterpart of peer-reviewed formal professional papers, but having less stringent limitations on manuscript length and extent of graphic presentations.
- **TECHNICAL MEMORANDUM.** Scientific and technical findings that are preliminary or of specialized interest, e.g., quick release reports, working papers, and bibliographies that contain minimal annotation. Does not contain extensive analysis.
- **CONTRACTOR REPORT.** Scientific and technical findings by NASA-sponsored contractors and grantees.

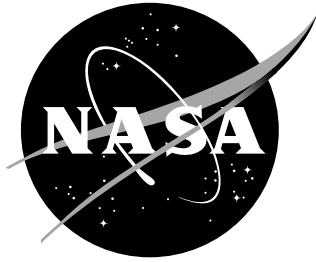
- **CONFERENCE PUBLICATION.** Collected papers from scientific and technical conferences, symposia, seminars, or other meetings sponsored or co-sponsored by NASA.
- **SPECIAL PUBLICATION.** Scientific, technical, or historical information from NASA programs, projects, and missions, often concerned with subjects having substantial public interest.
- **TECHNICAL TRANSLATION.** English-language translations of foreign scientific and technical material pertinent to NASA's mission.

Specialized services that complement the STI Program Office's diverse offerings include creating custom thesauri, building customized databases, organizing and publishing research results ... even providing videos.

For more information about the NASA STI Program Office, see the following:

- Access the NASA STI Program Home Page at <http://www.sti.nasa.gov>
- E-mail your question via the Internet to [help@sti.nasa.gov](mailto:help@sti.nasa.gov)
- Fax your question to the NASA STI Help Desk at (301) 621-0134
- Phone the NASA STI Help Desk at (301) 621-0390
- Write to:  
NASA STI Help Desk  
NASA Center for AeroSpace Information  
7121 Standard Drive  
Hanover, MD 21076-1320

NASA/CR-2000-210102



# Implementation of Advanced Two Equation Turbulence Models in the USM3D Unstructured Flow Solver

*Qunzhen Wang, Steven J. Massey, and Khaled S. Abdol-Hamid*  
*Analytical Services & Materials Inc., Lancaster, CA*

National Aeronautics and  
Space Administration

Langley Research Center  
Hampton, Virginia 23681-2199

Prepared for Langley Research Center  
under Contract NAS4-50066

---

April 2000

---

Available from:

NASA Center for AeroSpace Information (CASI)  
7121 Standard Drive  
Hanover, MD 21076-1320  
(301) 621-0390

National Technical Information Service (NTIS)  
5285 Port Royal Road  
Springfield, VA 22161-2171  
(703) 605-6000



# Implementation of Advanced Two Equation Turbulence Models in the USM3D Unstructured Flow Solver

Qunzhen Wang, Steven J. Massey & Khaled S. Abdol-Hamid  
*Analytical Services & Materials Inc.*  
*Lancaster, CA*

October 29, 1998

## Abstract

USM3D is a widely-used unstructured flow solver for simulating inviscid and viscous flows over complex geometries. The current version (version 5.0) of USM3D, however, does not have advanced turbulence models to accurately simulate complicated flow. We have implemented two modified versions of the original Jones and Launder  $k$ - $\varepsilon$  two-equation turbulence model and the Girimaji algebraic Reynolds stress model in USM3D. Tests have been conducted for three flat plate boundary layer cases, a RAE2822 airfoil and an ONERA M6 wing. The results are compared with those from direct numerical simulation, empirical formulae, theoretical results and the existing Spalart-Allmaras one-equation model.

## 1 Introduction

The unstructured-grid methodology offers some significant advantages compared to the traditional structured-grid method for simulating flows over complex aerodynamic shapes. This is mainly due to the promise that the construction of an unstructured grid around complex configurations, such as aircraft, requires much less time than a comparable block-structured grid. Furthermore, local refinement of unstructured grids can be carried out more easily to improve the accuracy of the simulation. While more work remains to be done to fully realize their potential, much progress has been made in modeling complicated flows on unstructured grids (see Mavriplis [1] for a review).

One important phenomenon for complex viscous flows is turbulence, which is difficult to simulate due to the existence of a wide range of scales. There are many types of methods to deal with turbulence, ranging from the simplest algebraic model to the most accurate direct numerical simulation. For most of the turbulence models, the Reynolds stress is assumed to be related to the mean strain rate by the eddy viscosity. Such turbulence models may be divided into zero-equation models (i.e., algebraic model), one-equation models, and two-equation models depending on the number of transport equations needed to be solved to obtain the eddy viscosity. The Reynolds stress model does not use the concept of eddy

viscosity. Instead, a transport equation for each component of the Reynolds stress tensor is solved directly. While the above models only solve the mean flow, large eddy simulations (LES) solve the large scale fluctuations in addition to the mean flow and only model the effects of small subgrid scales. Finally, the most accurate method is direct numerical simulation (DNS), where both the mean flow and all the fluctuations are solved directly.

While the Reynolds stress model, LES, and DNS methods are much more accurate than the eddy viscosity based method, they require prohibitive amounts of CPU time and memory. Therefore, the most widely used turbulence models in industry are still based on the concept of eddy viscosity. This is especially true for unstructured grid CFD codes. For example, the predominantly utilized turbulence model in the finite-element unstructured grid code of Mavriplis [2] is the algebraic model of Baldwin and Lomax [3], although extension has been made to include a two-equation model (Mavriplis and Martinelli [4]). The unstructured nodal-based finite volume code FUN3D (see Anderson [5], Anderson and Bonhaus [6]) contains two one-equation models, one by Baldwin and Barth [7] and the other by Spalart and Allmaras [8].

USM3D is a tetrahedral cell-centered unstructured flow solver for simulating inviscid and viscous flows over complex geometries. It was developed by Frink [9–12] at the NASA Langley Research Center and is now being widely used in both industry and government. This code is part of the TetrUSS flow analysis and design package which won the 1996 NASA Software of the Year award. USM3D utilizes a cell-centered, upwind-biased, finite-volume, implicit/explicit algorithm capable of solving the compressible Euler and Navier-Stokes equations on unstructured tetrahedral meshes. Like most other unstructured CFD codes, however, USM3D does not have advanced turbulence models to accurately simulate complex flows. The current production version of the code has only the one-equation turbulence model developed by Spalart and Allmaras [8], although a two equation  $k$ - $\varepsilon$  model was implemented in a previous research version of USM3D (Kwon and Hah [13]). It is well known that one-equation turbulence models are not adequate for complex flows such as separated or shear flows. The objective of this study is to present initial performance comparisons of the recently added advanced turbulence models with experimental data, theoretical results, DNS data, and the results from the existing Spalart-Allmaras one-equation model implemented by Frink [12].

## 2 Governing Equations

The integral form of the Navier-Stokes equations, which govern the compressible Newtonian fluid flow in the absence of external forces, can be written as

$$\frac{\partial}{\partial t} \iiint \mathbf{Q} dV + \iint \mathbf{F}(\mathbf{Q}) \cdot \hat{n} dS = \iint \mathbf{G}(\mathbf{Q}) \cdot \hat{n} dS \quad (1)$$

where the first term (time changing rate) is integrated over the volume of a bounded domain while the second term (convection) and the third term (diffusion) are integrated over the boundary of this domain. The quantities  $\mathbf{Q}$ ,  $\mathbf{F}(\mathbf{Q})$  and  $\mathbf{G}(\mathbf{Q})$  are vectors with five components and Eq. (1) contains five equations corresponding to the conservation of mass,

momentum, and energy. The unknowns in Eq. (1) are

$$\mathbf{Q} = \begin{bmatrix} \rho \\ \rho u \\ \rho v \\ \rho w \\ e \end{bmatrix} \quad (2)$$

where  $\rho$ ,  $u$ ,  $v$ ,  $w$  and  $e$  are density, three velocity components, and total energy, respectively. The inviscid flux is

$$\mathbf{F}(\mathbf{Q}) \cdot \hat{n} = \begin{bmatrix} \rho \\ \rho u \\ \rho v \\ \rho w \\ e + p \end{bmatrix} + p \begin{bmatrix} 0 \\ \hat{n}_x \\ \hat{n}_y \\ \hat{n}_z \\ 0 \end{bmatrix} \quad (3)$$

where  $p$  is the pressure and  $\hat{n}_x$ ,  $\hat{n}_y$ , and  $\hat{n}_z$  are Cartesian components of the exterior surface unit normal  $\hat{n}$  on the boundary of the domain. The viscous flux is

$$\mathbf{G}(\mathbf{Q}) \cdot \hat{n} = \frac{M_\infty}{Re_L} (\hat{n}_x G_1 + \hat{n}_y G_2 + \hat{n}_z G_3) \quad (4)$$

where

$$G_i = \begin{bmatrix} 0 \\ \tau_{i1} \\ \tau_{i2} \\ \tau_{i3} \\ u_j \tau_{ij} - q_i \end{bmatrix} \quad (5)$$

$M_\infty$  is the free-stream Mach number and  $Re_L$  is the Reynolds number based on a typical length scale (e.g., the total length of the flat plate).

The total stress  $\tau_{ij}$  and heat flux  $q_i$  can be divided into a laminar part (denoted by superscript  $L$ ) and a turbulence part (denoted by superscript  $T$ )

$$\tau_{ij} = \tau_{ij}^L + \tau_{ij}^T \quad (6)$$

$$q_i = q_i^L + q_i^T \quad (7)$$

with the laminar part being

$$\tau_{ij}^L = \mu^L \left[ \left( \frac{\partial u_i}{\partial x_j} + \frac{\partial u_j}{\partial x_i} \right) - \frac{2}{3} \delta_{ij} \frac{\partial u_k}{\partial x_k} \right] \quad (8)$$

$$q_i^L = - \frac{\mu^L}{(\gamma - 1) \text{Pr}^L} \frac{\partial T}{\partial x_i} \quad (9)$$

where  $\mu^L$  is the molecular viscosity,  $T$  is the temperature,  $\text{Pr}^L$  is the molecular Prandtl number, and  $\gamma = 1.4$  is the ratio of specific heats. Following Eqs. (8) and (9), the Reynolds stress and turbulent heat flux can be approximated as

$$\tau_{ij}^T = \mu^T \left[ \left( \frac{\partial u_i}{\partial x_j} + \frac{\partial u_j}{\partial x_i} \right) - \frac{2}{3} \delta_{ij} \frac{\partial u_k}{\partial x_k} \right] - \frac{2}{3} \rho k \delta_{ij} \quad (10)$$

$$q_i^T = -\frac{\mu^T}{(\gamma - 1)\text{Pr}^T} \frac{\partial T}{\partial x_i} \quad (11)$$

Note that the last term in Eq. (10) is presented only when a transport equation for turbulent kinetic energy  $k$  is solved.

## 2.1 Transport Equations for $k$ and $\varepsilon$

In the  $k$ - $\varepsilon$  model, two transport equations for the turbulent kinetic energy  $k$  and the dissipation rate  $\varepsilon$  are solved. The eddy viscosity,  $\mu^T$  in Eqs. (10) and (11), is then calculated based on  $k$  and  $\varepsilon$

$$\mu^T = C_\mu f_\mu \rho \frac{k^2}{\varepsilon} \quad (12)$$

where  $f_\mu$  is a damping function and  $C_\mu = 0.09$ . The transport equation for  $k$  is

$$\frac{\partial \rho k}{\partial t} + \frac{\partial \rho k u_j}{\partial x_j} - \frac{\partial}{\partial x_j} \left[ \mu_k \frac{\partial k}{\partial x_j} \right] \frac{M_\infty}{Re_L} = S_k \quad (13)$$

where

$$S_k = \overline{P} \frac{M_\infty}{Re_L} - \rho(1 + \Gamma) \varepsilon \frac{Re_L}{M_\infty} \quad (14)$$

$$\overline{P} = \tau_{ij}^T \frac{\partial u_i}{\partial x_j} \quad (15)$$

$$\mu_k = \mu^L + \frac{\mu^T}{\sigma_k} \quad \sigma_k = 1.0 \quad (16)$$

Similarly, the transport equation for  $\varepsilon$  can be written as

$$\frac{\partial \rho \varepsilon}{\partial t} + \frac{\partial \rho \varepsilon u_j}{\partial x_j} - \frac{\partial}{\partial x_j} \left[ \mu_\varepsilon \frac{\partial \varepsilon}{\partial x_j} \right] \frac{M_\infty}{Re_L} = S_\varepsilon \quad (17)$$

$$S_\varepsilon = C_{\varepsilon 1} \overline{P} \frac{\varepsilon}{k} \frac{M_\infty}{Re_L} - C_{\varepsilon 2} f_2 \frac{\varepsilon}{k} \frac{Re_L}{M_\infty} \left[ \rho \varepsilon - L_k \left( \frac{M_\infty}{Re_L} \right)^2 \right] \quad (18)$$

$$L_k = 2\mu^L \left[ \left( \frac{\partial \sqrt{k}}{\partial x} \right)^2 + \left( \frac{\partial \sqrt{k}}{\partial y} \right)^2 + \left( \frac{\partial \sqrt{k}}{\partial z} \right)^2 \right] \quad (19)$$

$$\mu_\varepsilon = \mu^L + \frac{\mu^T}{\sigma_\varepsilon} \quad \sigma_\varepsilon = 1.3 \quad C_{\varepsilon 1} = 1.44 \quad C_{\varepsilon 2} = 1.92 \quad (20)$$

$$f_2 = 1 - 0.3 \exp(-R_t^2) \quad R_t = \frac{\rho k^2}{\mu^L \varepsilon} \quad (21)$$

In all the equations as well as all the figures shown in this paper, unless stated explicitly otherwise, the length is normalized by a characteristic length  $L$ , the velocity by  $a_\infty$ , the density by  $\rho_\infty$ , the viscosity by  $\mu_\infty$ , the turbulent kinetic energy  $k$  by  $a_\infty^2$ , and the dissipation rate  $\varepsilon$  by  $\rho_\infty a_\infty^4 / \mu_\infty$ , where  $a_\infty$  is the free-stream speed of sound,  $\rho_\infty$  is the free-stream density, and  $\mu_\infty$  is the free-stream molecular viscosity.

The compressibility correction  $\Gamma$  in Eq. (14) and the damping function  $f_\mu$  in Eq. (12) can take different forms. The two most widely used compressibility corrections are the Sarkar *et al.* [14] model

$$\Gamma = M_t^2 \quad (22)$$

and the Wilcox [15] model

$$\Gamma = (M_t^2 - M_{t0}^2) H(M_t - M_{t0}) \quad (23)$$

where  $H(x)$  is the Heaviside step function, the turbulent Mach number  $M_t = \sqrt{k}/a$  with  $a$  being the local speed of sound. The damping function could take one of the following three forms:

a) Jones and Launder [16] form

$$f_\mu = \exp \left[ -\frac{3.41}{(1 + \frac{R_t}{50})^2} \right] \quad (24)$$

b) Van Driest form (Nagano and Hishida [17])

$$f_\mu = 1 - \exp \left( \frac{-n^+}{A^+} \right) \quad (25)$$

c) Speziale *et al.* [18] form

$$f_\mu = \left( 1 + \frac{3.45}{\sqrt{R_t}} \right) \tanh \left( \frac{n^+}{70} \right) \quad (26)$$

For the results shown in this paper, `ivisc=6` refers to the Jones and Launder form of the damping function, Eq. (24), with no compressibility correction (i.e.,  $\Gamma = 0$ ) and `ivisc=7` refers to the Jones and Launder model modified by Carlson [19] as given in Eqs. (27-31).

$$\kappa = 0.41 \quad \alpha = 1.15 \quad C_{\varepsilon 2} = 1.9 \quad (27)$$

$$C_{\varepsilon 1} = \alpha \left( 1 + 0.2174 \frac{P}{\varepsilon} \right) \quad (28)$$

$$C_1 = \alpha \left( 1 + 0.2174 \frac{1.5}{\varepsilon} \right) \quad (29)$$

$$\sigma_\varepsilon = \frac{\kappa^2}{(C_{\varepsilon 2} - C_1) \sqrt{C_\mu}} \quad (30)$$

$$f_\mu = \exp \left[ -\frac{6}{(1 + \frac{R_t}{75})^2} \right] \quad (31)$$

The  $k$ - $\varepsilon$  model discussed above is the standard model, which is also called the “linear model” because the turbulent stress is linearly related to the mean strain rate by the eddy viscosity as is clear from Eq.(10).

## 2.2 Algebraic Reynolds Stress Model

Various direct numerical simulation (DNS) data have shown that the turbulent stress does not vary linearly with the mean strain rate. A more accurate representation is the Reynolds stress model where a transport equation for each component of the Reynolds stress tensor is solved directly and the concept of eddy viscosity is not used. However, the Reynolds stress model requires a tremendous amount of CPU time and computer memory and thus, is seldom used in complex engineering applications. The algebraic stress model, in which a nonlinear term is added to the turbulent stress (so it is also called the “nonlinear model”), offers a practical compromise. Following Girimaji [20], the turbulent stress in the algebraic stress model is

$$\tau_{ij}^T = \mu^T \left[ S_{ij} - \frac{1}{3} \delta_{ij} \frac{\partial u_k}{\partial x_k} \right] - \frac{2}{3} \rho k \delta_{ij} + 2\mu^T K_1 \frac{k}{\varepsilon} [S_{ik} W_{kj} - W_{ik} S_{kj}] + 2\mu^T K_2 \frac{k}{\varepsilon} \left[ S_{ik} S_{kj} - \frac{1}{3} S_{kl} S_{lk} \right] \quad (32)$$

where the mean strain rate and mean vorticity are

$$S_{ij} = \frac{1}{2} \left( \frac{\partial u_i}{\partial x_j} + \frac{\partial u_j}{\partial x_i} \right) \quad (33)$$

$$W_{ij} = \frac{1}{2} \left( \frac{\partial u_i}{\partial x_j} - \frac{\partial u_j}{\partial x_i} \right) \quad (34)$$

respectively. In Eq.(32),  $K_1$  and  $K_2$  are given by

$$K_1 = \frac{G_2}{G_1} \quad K_2 = \frac{G_3}{G_1} \quad (35)$$

while  $G_1$  can be obtained from

$$G_1 = \begin{cases} \frac{-L_1^0 L_2}{(L_0^1)^2 + 2\eta_2 (L_4)^2} & \eta_1 = 0 \\ \frac{-L_1^0 L_2}{\frac{2}{3}\eta_1 (L_3)^2 + (L_0^1)^2 + 2\eta_2 (L_4)^2} & L_1^1 = 0 \\ \frac{\frac{p}{3} + \left(-\frac{b}{2} + \sqrt{D}\right)^{\frac{1}{3}} + \left(-\frac{b}{2} - \sqrt{D}\right)^{\frac{1}{3}}}{\frac{p}{3} + 2\sqrt{-\frac{a}{3}} \cos\left(\frac{\theta}{3}\right)} & D > 0 \\ \frac{\frac{p}{3} + 2\sqrt{-\frac{a}{3}} \cos\left(\frac{\theta}{3}\right)}{\frac{p}{3} + 2\sqrt{-\frac{a}{3}} \cos\left(\frac{\theta}{3} + \frac{2\pi}{3}\right)} & D < 0, b < 0 \\ \frac{\frac{p}{3} + 2\sqrt{-\frac{a}{3}} \cos\left(\frac{\theta}{3} + \frac{2\pi}{3}\right)}{\frac{p}{3} + 2\sqrt{-\frac{a}{3}} \cos\left(\frac{\theta}{3}\right)} & D < 0, b > 0 \end{cases} \quad (36)$$

and  $G_2$  and  $G_3$  are

$$G_2 = \frac{-L_4 G_1}{L_0^1 - \eta_1 L_1^1 G_1} \quad (37)$$

$$G_3 = \frac{2L_3 G_1}{L_0^1 - \eta_1 L_1^1 G_1} \quad (38)$$

where

$$\eta_1 = \frac{k^2}{\varepsilon} S_{ij} S_{ij} \left( \frac{M_\infty}{Re_L} \right)^2 \quad (39)$$

$$\eta_2 = \frac{k^2}{\varepsilon} W_{ij} W_{ij} \left( \frac{M_\infty}{Re_L} \right)^2 \quad (40)$$

$$p = \frac{2L_1^0}{\eta_1 L_1^1} \quad (41)$$

$$r = \frac{L_2 L_1^0}{(\eta_1 L_1^1)^2} \quad (42)$$

$$q = \frac{(L_1^0)^2 + \eta_1 L_2 L_1^1 - \frac{2}{3} \eta_1 (L_3)^2 + 2\eta_2 (L_4)^2}{(\eta_1 L_1^1)^2} \quad (43)$$

$$a = q - \frac{p^2}{3} \quad (44)$$

$$b = \frac{1}{27} (2p^3 - 9pq + 27r) \quad (45)$$

$$D = \frac{b^2}{4} + \frac{a^3}{27} \quad (46)$$

$$\cos \theta = \frac{-b/2}{\sqrt{-a^3/27}} \quad (47)$$

$$L_0^1 = \frac{C_1^0}{2} - 1 \quad (48)$$

$$L_1^1 = C_1^1 + 2 \quad (49)$$

$$L_2 = \frac{C_2}{2} - \frac{2}{3} \quad (50)$$

$$L_3 = \frac{C_3}{2} - 1 \quad (51)$$

$$L_4 = \frac{C_4}{2} - 1 \quad (52)$$

$$C_1^0 = 3.4 \quad C_1^1 = 1.8 \quad C_2 = 0.36 \quad C_3 = 1.25 \quad C_4 = 0.4 \quad (53)$$

Furthermore, instead of  $C_\mu = 0.09$  for the linear model,  $C_\mu = -G_1$  is applied in the nonlinear model, which is invoked by setting `ivisc=6` with `inl=7` instead of `inl=0`.

### 3 Numerical Procedure

The details of the numerical procedure for solving equation (1) are discussed in Frink [10–12] and only a brief overview is given here. The spatial computational domain is divided into a finite number of tetrahedral cells and a finite-volume discretization is applied to each cell. This procedure results in a set of volume-averaged state variables  $\mathbf{Q}$  which are in balance with the area-averaged inviscid flux  $\mathbf{F}(\mathbf{Q})$  and viscous flux  $\mathbf{G}(\mathbf{Q})$ . Inviscid fluxes are obtained across each cell face using either the Roe [21] flux-difference splitting approach or the Van Leer [22] flux-vector splitting technique. The data at nodal points could be obtained from the cell-averaged data by either an inverse-distance weighted averaging scheme or a Laplacian-weighted averaging scheme. The viscous fluxes are approximated at the cell-face centroids by linear reconstruction. An implicit time integration algorithm using the linearized backward

Euler time differencing approach is applied to update the solution. The resulting linear system of equations are solved at each time step with a subiterative procedure by a point-Jacobi method. Convergence to the steady state solution is accelerated by advancing the equations at each cell in time by the maximum permissible time step in that cell. The CFL number is scaled according to the deviation of cell aspect ratio from the ideal value of an isotropic tetrahedron.

The solution procedure for the two turbulence transport equations (13) and (17) are similar to that for solving the Navier-Stokes equations. Equations (13) and (17) are solved separately from the flow governing equations and from each other using the same backward Euler time integration scheme. The  $k$  and  $\varepsilon$  equations can be solved using either first-order or second-order schemes. For the second-order method, either Roe's SuperBee limiter or the Minimum Modulus (Min-Mod) limiter can be applied. To allow a large CFL number, an implicit time-stepping method is used to solve the  $k$  and  $\varepsilon$  equations.

Equations (13) and (17) are written in conservative form. There are two other forms of the transport equations: non-conservative form and incompressible form. For example, these three forms of the  $k$  equation can be written as

$$\text{conservative (iconf=1)} \quad \frac{\partial \rho k}{\partial t} + \frac{\partial \rho k u_j}{\partial x_j} - \frac{\partial}{\partial x_j} \left[ \mu_k \frac{\partial k}{\partial x_j} \right] \frac{M_\infty}{Re_L} = S_k \quad (54)$$

$$\text{non-conservative (iconf=0)} \quad \frac{\partial k}{\partial t} + \frac{\partial u_j k}{\partial x_j} - \frac{\partial}{\partial x_j} \left[ \frac{\mu_k}{\rho} \frac{\partial k}{\partial x_j} \right] \frac{M_\infty}{Re_L} = \frac{S_k}{\rho} \quad (55)$$

$$\text{incompressible (iconf=-1)} \quad \frac{\partial k}{\partial t} + u_j \frac{\partial k}{\partial x_j} - \frac{\partial}{\partial x_j} \left[ \frac{\mu_k}{\rho} \frac{\partial k}{\partial x_j} \right] \frac{M_\infty}{Re_L} = \frac{S_k}{\rho} \quad (56)$$

All three forms can be used to solve the  $k$  and  $\varepsilon$  equations in USM3D (see § 4.1 for a comparison of the results). In general, the conservative form of Eq. (54) yields more accurate solutions than the other two forms, while the incompressible form of Eq. (56) is the least accurate since it is only applicable for incompressible flow.

Two input parameters  $k_0$  and  $\mu_0^T$  are needed to specify the initial conditions and limit the smallest values of  $k$  and  $\varepsilon$ . The initial conditions are  $k = k_0$  and  $\varepsilon = \varepsilon_0 = C_\mu \rho k_0^2 / \mu_0^T$ . The turbulent kinetic energy and dissipation rate are not allowed to become smaller than  $k_0$  and  $\varepsilon_0$ , respectively. On solid surfaces, the boundary conditions are  $k = k_0$  and  $\varepsilon = L_k / \rho (M_\infty / Re_L)^2$ . Far field boundary conditions are applied by extrapolating  $k$  and  $\varepsilon$  from the interior for outflow boundaries and taken from the free-stream for the inflow boundaries.

The  $k$ - $\varepsilon$  model has been coupled with wall function formulations to reduce the need for grid-resolving the flow in the near wall region. The following three different wall functions can be used together with the  $k$ - $\varepsilon$  model: (1) **iwallf=1**: the original wall function developed by Frink [12]; (2) **iwallf=2**: a wall function similar to that used in PAB3D (see Abdol-Hamid *et al.* [23] for details); (3) **iwallf=3**: same as the original wall function except the velocity components are zero at the solid surface. For **iwallf=1**, a slip velocity boundary condition is obtained by solving the Spalding formula

$$y^+ = u^+ + e^{-\kappa B} \left[ e^{\kappa u^+} - 1 - \kappa u^+ - \frac{(\kappa u^+)^2}{2} - \frac{(\kappa u^+)^3}{6} \right] \quad (57)$$



with  $\kappa = 0.4$  and  $B = 5.5$  using the Newton-Raphson iteration method while the velocity at the solid boundary for `iwallf=2` and `iwallf=3` is zero.

## 4 Results

### 4.1 Flat Plate Cases: BLT2, BLT3, BLT4

Three tetrahedral grids for a simple flat plate boundary layer have been generated using the grid generator VGRID (Pirzadeh [24]). For each of the grids, results of the newly added  $k - \varepsilon$  models are compared with the existing Spalart-Allmaras model and with experimental and theoretical data, (including DNS data) for the “wall function” grid, BLT2, and for the non-linear ARSM results on the near-wall resolved grids, BLT3 and BLT4. The computational domain extends from  $x = -0.5$  to  $x = 1.0$  in the streamwise direction, from  $y = -0.02$  to  $y = 0.02$  in the spanwise direction for BLT3 and BLT4, ( $-0.05 < y < 0.05$  for BLT2), and from  $z = 0$  to  $z = 0.22$  in the wall normal direction. The free-stream Mach number is  $M_\infty = 0.5$  and Table 1 shows the Reynolds number for each case. In addition, Table 1 shows the grid size and minimum  $y^+$  values. The grids for the flat plate cases are shown in Figures 1-3.

Table 1: Summary of flat plate cases.

Case	Cells	Nodes	Faces	B. Nodes	B. Faces	$Re_L$	$y^+$
BLT2	48,497	9,629	99,805	2,813	5,612	$2 \times 10^6$	223
BLT3	37,483	8,038	78,328	3,364	6,724	$2 \times 10^6$	1.8
BLT4	43,912	9,321	91,594	3,772	7,540	$20 \times 10^6$	1.5

There are four cells in the spanwise direction for BLT2 and two cells for the BLT3 and BLT4 grids. Near the wall, the grid spacings for the BLT3 and BLT4 grids are much smaller than that for BLT2, but the grid spacings for BLT3 and BLT4 are much larger than that for BLT2 far away from the wall. For BLT3 and BLT4, the first node point away from the wall has a  $y^+ \approx 1.8$  and  $1.5$  respectively, while for the BLT2 grid  $y^+ \approx 223$  at  $x/L = 0.5$ . Therefore, a wall function has to be applied for BLT2 while no wall function is needed for BLT3 or BLT4. Sample input files for the three plate cases are in Appendices A, B, and C.

#### 4.1.1 BLT2 Flat Plate - Wall Function Case

The CFL number and residual history of the governing equations using the Spalart-Allmaras and linear  $k - \varepsilon$  models are shown in Figure 4. The residual history for the Spalart-Allmaras and Carlson modified  $k - \varepsilon$  model both converge rapidly at nearly the same rate to a level of 9 orders of magnitude smaller than the initial residual. The first linear model (`ivisc=6`) converged much slower after the 500<sup>th</sup> time step and only decreased by less than 4 orders of magnitude after 4,000 time steps. The CFL number is allowed to increase dynamically from 1 to 200 according to the residual; it increases when the residual is decreasing and decreases when the residual is increasing. For each of the three models tested, the CFL number rapidly increased to its maximum value within 40 time steps and remained at 200 for the duration of the run indicating a robust convergence. In Figure 5, velocity profiles are compared with

the empirical formula of Spalding, Eq. (57), while the skin friction coefficient is compared with the theoretical values for fully turbulent flow.

$$C_f = 0.0583(\text{Re}_x)^{-1/5} \quad (58)$$

It is evident that  $u^+$  from the second (`ivisc=7`)  $k$ - $\varepsilon$  model is the closest to Spalding's formula with the Spalart-Allmaras results the next closest. The first  $k$ - $\varepsilon$  model initially matches the data as dictated by the wall function, but then significantly under predicts  $u^+$ . The skin friction coefficient from the first  $k$ - $\varepsilon$  model is significantly larger than the theoretical value whereas the Spalart-Allmaras model gives a result slightly smaller than the theoretical value and the second  $k$ - $\varepsilon$  model initially matches theory closely before predicting a slightly larger value.

In summary, for the coarse flat plate grid using a wall function, (BLT2), the Carlson modified linear  $k$ - $\varepsilon$  model performed the best, with the Spalart-Allmaras model nearly as good and the first  $k$ - $\varepsilon$  model not in good agreement with empirical or theoretical data. The CPU time per timestep per cell on an Intel Pentium II 300 MHz was  $229\mu\text{sec}$  for the Spalart-Allmaras model and 13% more for the linear  $k$ - $\varepsilon$  models.

#### 4.1.2 BLT3 Flat Plate - Grid Resolved Case

The CFL number and the residual of the governing equations using the Spalart-Allmaras and linear  $k$ - $\varepsilon$  models are shown in Figure 6. The residual history for all three models converge rapidly at roughly the same rate to a level of 5 orders of magnitude smaller than the initial residual. The temporary hump in the residual trace around  $n = 1000$  is characteristic of the establishment of turbulence for a non-wall function grid. For each of the three models tested, the CFL number rapidly increased to its maximum value within 75 time steps and remained at 200 for the duration of the run indicating a robust convergence.

Inspection of the velocity profile and skin friction plots, see Figure 7, confirms that for the BLT3 grid a wall function is not needed. It is evident that  $u^+$  from the Spalart-Allmaras model is closer to the Spalding curve with the second  $k$ - $\varepsilon$  model under predicting  $u^+$  slightly and the first  $k$ - $\varepsilon$  model under predicting significantly. The skin friction coefficient from the first  $k$ - $\varepsilon$  model is significantly larger than the theoretical value whereas the Spalart-Allmaras model gives a result slightly smaller than the theoretical value and the second  $k$ - $\varepsilon$  model matches theory the closest predicting a slightly larger value.

The turbulent kinetic energy and dissipation rate from the first  $k$ - $\varepsilon$  model (`ivisc=6`) at different downstream locations are compared with those from the DNS work of Spalart [25] in Figure 8. The turbulent kinetic energy  $k$  has been normalized by  $(u^*)^2$ , where  $u^*$  is the friction velocity, while dissipation rate  $\varepsilon$  has been normalized by  $\rho_\infty(u^*)^4/\mu_\infty$ . The profiles of both  $k$  and  $\varepsilon$  at different downstream locations are very similar. The turbulent kinetic energy has a peak at  $y^+ \approx 20$  since  $k = 0$  both at the wall and at the free stream. Although the peak value from the first  $k$ - $\varepsilon$  model is smaller than that from DNS, the overall agreement is good. There is no peak for the dissipation rate since  $\varepsilon$  is the largest at the wall. The dissipation rate from the first  $k$ - $\varepsilon$  model also agrees well with that from DNS.

The Reynolds stress components from the first  $k$ - $\varepsilon$  model are compared with those from the DNS of Spalart [25] in Figure 9. Similar to the turbulent kinetic energy, the Reynolds stress components have been normalized by  $(u^*)^2$ . The Reynolds shear stress from the first

$k$ - $\varepsilon$  model agrees well with that from DNS. The three normal stress components from the first  $k$ - $\varepsilon$  model are almost identical whereas the streamwise component from DNS is much larger than the other two components. This is a property of the linear model, where the Reynolds stress is assumed to be isotropic. These three components will be different after we implement the nonlinear model (i.e., the algebraic stress model) by adding an extra nonlinear term in the right hand side of equation (10). Note that the normal stress components,  $ww^+$ , from  $k$ - $\varepsilon$  model in Figure 9(b) are very close to  $2/3k$  from Figure 8(a) because the first term in the right hand side of equation (10) is much smaller than the second term. Although not shown here, the three normal stress components from the Spalart-Allmaras model are nearly zero since the turbulent kinetic energy is not modeled (i.e., there is no  $2/3k$  term in equation (10) for this model).

As discussed in § 3, the transport equations for  $k$  and  $\varepsilon$  can be solved in three different forms: conservative, nonconservative and incompressible form. Figure 10 compares the residual history and streamwise velocity in wall coordinates from these forms. It is clear that the difference between the conservative and nonconservative forms is very small for this case. The residual from the incompressible form is much larger than the other two forms while the streamwise velocity from these three forms are similar.

Although turbulent solutions can be obtained for the linear  $k$ - $\varepsilon$  models using an initial eddy viscosity of  $\mu^T/\mu^L = 1$ , it was found that this initial condition caused the boundary layer flow to remain laminar when used as the initial condition for the algebraic stress model. Therefore, the initial condition of  $\mu^T/\mu^L = 10$  was used for all algebraic stress cases. Figure 11 shows the residual of the Navier-Stokes equations using the algebraic stress model with  $\mu^T/\mu^L = 10$  for the flat plate boundary layer with the BLT3 grid. A great deal of oscillations occur and the residual settles down at about 0.75 orders of magnitude smaller than the initial residual after about 1,900 steps. Note that this residual is much larger than those from the first linear  $k$ - $\varepsilon$  model as well as the Spalart-Allmaras model in Figure 6.

The skin friction coefficient and the streamwise velocity in wall coordinates from the nonlinear algebraic stress model are compared with those from the linear  $k$ - $\varepsilon$  model in Figure 12(a). The streamwise velocity component from the nonlinear algebraic stress model agrees with Spalding's empirical formula better than that from the first linear  $k$ - $\varepsilon$  model (`ivisc=6`). The skin friction coefficient from the algebraic stress model also has a better agreement with the theoretical value than that from the first linear  $k$ - $\varepsilon$  model from  $x \approx 0.1$  to  $x \approx 0.5$ , at which point the linear model is more accurate.

Since the success of the algebraic stress model depends on the initial condition, we ran a case where the algebraic stress model was restarted from the solution of the first linear  $k$ - $\varepsilon$  model. The skin friction coefficient and the streamwise velocity in wall coordinates from this run are shown in Figure 13. Similar to those shown in Figure 12, the streamwise velocity component agrees better with the Spalding empirical formula than that from the first linear  $k$ - $\varepsilon$  model while the skin friction coefficient also has a better agreement with the theoretical value than that from the first linear  $k$ - $\varepsilon$  model from  $x \approx 0.1$  to  $x \approx 0.5$ , after which, the linear model is more accurate.

In summary, for the BLT3 refined flat plate grid without using a wall function, the Carlson modified linear  $k$ - $\varepsilon$  model performed best for predicting skin friction and is a close second to Spalart-Allmaras for velocity profile. Experience with the linear models in the structured code PAB3D [23] indicates that with grid refinement the accuracy of the linear models

will improve significantly. The CPU time per timestep per cell on an SGI with two IP30 processors was  $194\mu\text{sec}$  for the Spalart-Allmaras model and 10% more for the linear  $k-\varepsilon$  models. As discussed above, the residuals for the BLT2 and BLT3 grids using the algebraic stress model do not drop as much as those of the first linear  $k-\varepsilon$  and the Spalart-Allmaras models. Although both skin friction coefficient and streamwise velocity distributions from the algebraic stress model are better than those of the first linear  $k-\varepsilon$  model, the results are still not as accurate as the Spalart-Allmaras model. Furthermore, the results from the algebraic stress model depend on the initial condition. In an effort to decrease the streamwise distance needed for a turbulent boundary layer to develop, a high Reynolds number version of the BLT3 grid is examined in the following section.

#### 4.1.3 BLT4 Flat Plate

The BLT4 grid was designed as a high Reynolds number counterpart to the BLT3 grid. It has a first nodal point normal distance of  $1/10$  of the BLT3 grid and was run with a Reynolds number is 20 million instead of 2 million. The CFL number and the residual of the governing equations using the Spalart-Allmaras, both linear  $k-\varepsilon$  models and the Girimaji algebraic Reynolds stress model are shown in Figure 14. The residual history for all cases except for the ARSM converge rapidly down 4 orders of magnitude, with the linear  $k-\varepsilon$  models converging less robustly than the Spalart-Allmaras model. In this case, the nonlinear model was run without using a linear solution as the initial condition, and despite setting the CFL number to a low constant value of 50 and running it for 8,000 iterations, the residual never settled down. The CFL number for the Spalart-Allmaras and second linear models rapidly increased to its maximum value within 60 time steps while the first linear model initially increased then temporarily dipped to 25 around  $n = 120$  before reaching the maximum allowable CFL at  $n = 160$ .

Inspection of the velocity profile and skin friction plots, see Figure 15, confirms that for the BLT4 grid a wall function is not needed. It is evident that for this grid the Spalart-Allmaras model is the closest to the experimental and theoretical data. The first linear model performs the worst and the second linear model and the ARSM are positioned between the other two, with the second linear model slightly closer to data than the ARSM. It is expected that with grid refinement and in less ideal configurations, the performance of the linear models and especially the nonlinear model will improve significantly. The CPU time per timestep per cell on an Intel Pentium II 300 MHz was  $213\mu\text{sec}$  for the Spalart-Allmaras model, 13% more for the linear  $k-\varepsilon$  models and 37% more for the non-linear model with `nstagek=5`.

## 4.2 RAE2822 Airfoil

In this section results for the previously mentioned turbulence models of Spalart-Allmaras model, linear  $k-\varepsilon$  (`ivisc=6`), and linear  $k-\varepsilon$  (`ivisc=7`) will be compared with the Girimaji algebraic Reynolds stress model (ARSM), as well as, the experimental results of case 10 of Cook *et al.* [26] for a transonic airfoil. A sample input file is shown in Appendix D.

The computational domain extends 6 chord lengths away from the airfoil in all directions with a channel width of  $0.2c$  spanning 2 cells. The free-stream Mach number of the boundary

layer, Reynolds number, and corrected free air angle-of-attack is  $M_\infty = 0.75$ ,  $Re = 6.2 \times 10^6$  and  $\alpha = 2.81^\circ$ , respectively. The grid contains 29,976 cells, 8,477 nodes, 66,772 faces, 6,820 boundary nodes, and 13,640 boundary faces. The distance of the first node away from the wall corresponds to  $y^+ \approx 0.8$ . Full and closeup views of the grid are shown in Figure 16.

Unlike the previous flat plate cases, the residual and CFL history (Figure 17) are much noisier, which may be due to unsteadiness in the region behind the shock. All of the models converge between 3 and 3.5 orders of magnitude after 4,000 time steps. Initially, the ARSM shows a great deal of oscillation since it is more dependent on the initial condition. Also, observed is a large increase in residual for the second linear model before finally settling down. The CFL history reveals that for the first 400 time steps each model is behaving similarly with the exception of the ARSM whose CFL history appears to be shifted to the left. After  $n = 400$ , the CFL number for all models oscillate periodically at high frequency.

Lift and drag coefficient histories are shown in Figure 18. From the history plots, it is evident that the Spalart-Allmaras, first linear  $k-\varepsilon$ , and Girimaji models follow the same convergence trend while the second linear model oscillates much more before settling down at around  $n = 2,500$ . The results at  $n = 4,000$  along with experimental data and results from PAB3D for the first linear model are compared in Table 2. Final results show that the Spalart-Allmaras model is in closest agreement with experimental data. The next best results for USM3D are produced by the first linear model, the ARSM, and finally the second linear model. As an indicator of grid dependence for the advanced models, results in good agreement with experimental data from PAB3D are shown for the first linear model.

In Figure 19, the predicted pressure coefficient from each model is plotted with the experimental data of Cook [26]. All models miss the location of the first suction peak by approximately  $0.02c$ . This is likely due to the fact that the current implementation of the turbulence models in USM3D does not allow for setting a trip location for the boundary layer, while in the experiment it was set to  $0.03c$ . Other areas of disagreement with experiment and among the models themselves is the shock location and region aft of the shock. The prediction of shock location by the second linear model was in excellent agreement while the other models all predicted different locations—all aft of the experimental location. Aft of the shock, all models predicted a lower  $C_P$  than experiment with the Girimaji model in the best agreement.

Table 2: Comparison of  $C_L$  and  $C_D$  with experimental data of Cook *et al.* [26] and PAB3D linear  $k-\varepsilon$  model (ivisc=6) [23].

Case	$C_L$	% diff	$C_D$	% diff
Experiment	0.743	—	0.0242	—
Spalart-Allmaras	0.732	-1.5	0.0214	-11.6
Linear $k-\varepsilon$ (ivisc=6)	0.691	-7.0	0.0199	-17.8
Linear $k-\varepsilon$ (ivisc=7)	0.649	-12.7	0.0178	-26.4
Girimaji ARSM	0.803	8.1	0.0293	21.1
PAB3D Linear $k-\varepsilon$ (ivisc=6)	0.720	-3.1	0.0257	6.2

### 4.3 ONERA M6 Wing

The tetrahedral viscous grid for the ONERA M6 wing was generated using VGRID and is similar in construction to those in Frink [12]. The grid contains 338,417 cells, 59,496 nodes, 682,257 faces, 5,425 boundary nodes and 10,846 boundary faces. On the wing surface the midchord  $y^+$  was approximately equal to 2 for the flow conditions of  $M_\infty = 0.8447$ ,  $Re_{mac} = 11.7 \times 10^6$  and  $\alpha = 5.06^\circ$ . The computational domain is bounded by a rectangular box defined by  $-6.5 \leq x \leq 6.5$ ,  $0 \leq y \leq 4$ , and  $-6.5 \leq z \leq 6.5$ , in aerodynamic coordinates relative to a semispan length of 1. Surface and symmetry plane meshes are shown in Figure 20.

For this ONERA M6 wing case, results are presented for the Spalart-Allmaras model and the second linear (`ivisc=7`) model with varying numbers of Jacobi iterations in the solution of the  $k$ - $\varepsilon$  equations. The current implementation of the ARSM was found to be very stiff for the relatively coarse wing grid. Further investigations need to be performed to identify the minimum grid density required for a stable solution in various flow regimes. A sample input file is included in Appendix E. In Figure 21, the residual history is seen to be fairly similar among the models with the Spalart-Allmaras being the smoothest. Both linear cases are more noisy until  $n = 500$ . To aid solution stability, the original CFL ramping scheme in USM3D was used to bring the CFL number to a constant value of 75, rather than letting it vary dynamically up to 200 as in previous cases.

In Figure 22, the coefficient of lift and drag histories confirm that the reduction in the number of iterations on the  $k$ - $\varepsilon$  equations causes no inaccuracy in the solution. This is significant because the reduction brings a 10% time savings. While the two linear cases agree with each other, the Spalart-Allmaras model predicts a 4% lower  $C_L$  while agreeing exactly with the linear models prediction of  $C_D$ .

Limiting surface streamlines simulating “oil-flow” patterns, shown in Figure 23, depict a significant amount of shock separated flow beyond the  $\eta \approx 0.65$  for both models with the Spalart-Allmaras model results showing the strongest separation. The  $C_P$  plots in Figure 24 demonstrate this with the exception of the  $\eta = 0.90$  plane where Spalart-Allmaras matches the shock location well. It should be noted however, that the solutions in the tip region,  $\eta > 0.90$ , can be particularly sensitive to a variety of factors such as grid density and turbulence model (see Rumsey and Vatsa [27]) and should be explored further in future studies.

The CPU time per timestep per cell on an SGI with two IP30 processors was 216  $\mu\text{sec}$  for the Spalart-Allmaras model, 223  $\mu\text{sec}$  for the second linear (`ivisc=7`)  $k$ - $\varepsilon$  model with 2 Jacobi iterations (`nstagek=2`) on the  $k$ - $\varepsilon$  equations and 249  $\mu\text{sec}$  for the second linear model with 6 Jacobi iterations.

In summary, the linear  $k$ - $\varepsilon$  model is seen to perform well in a complex three-dimensional flow with only a small increase in CPU time required over the existing Spalart-Allmaras model.

## 5 Concluding Remarks

A systematic study has been conducted to assess the accuracy of two newly implemented turbulence models, modified versions of the standard linear two-equation  $k$ - $\varepsilon$  model and the non-linear algebraic Reynolds stress model of Girimaji. Initial results of test cases for the

flat plate, airfoil, and wing indicate that the new two-equation models yield comparable accuracy and efficiency to that of the Spalart-Allmaras one-equation model. Work is currently underway to further examine factors such as grid sensitivities and solution details.

## 6 Acknowledgements

This research was sponsored by the Configuration Aerodynamics Branch, (CAB), of the NASA Langley Research Center. Supplemental computational resources were also generously provided by the sponsors.

## References

- [1] Mavriplis, D., “Unstructured-Grid Techniques,” *Ann. Rev. Fluid Mech.*, Vol. 29, 1997, pp. 473–514.
- [2] Mavriplis, D., “Turbulent Flow Calculation Using Unstructured and Adaptive Meshes,” *Int. J. Numer. Meth. Fluids*, Vol. 13, 1991, pp. 1131–1141.
- [3] Baldwin, B. and Lomax, H., “Thin Layer Approximation and Algebraic Model for Separated Turbulent Flows,” AIAA Paper 78-257.
- [4] Mavriplis, D. and Martinelli, L., “Multigrid Solution of Compressible Turbulent Flow on Unstructured Mesh Using a Two-Equation Model,” ICASE Technical Report 91-11.
- [5] Anderson, W., “A Grid Generation and Flow Solution Method for the Euler Equations on Unstructured Grids,” *Journal of Computational Physics*, Vol. 110, 1994, pp. 23–38.
- [6] Anderson, W. and Bonhaus, D., “An implicit upwind algorithm for computing turbulent flows on unstructured grids,” *Computers and Fluids*, Vol. 23, 1994, pp. 1–21.
- [7] Baldwin, B. and Barth, T., “A One-Equation Turbulence Transport Model for High Reynolds Number Wall Bounded Flows,” NASA Technical Memorandum 102847, 1978.
- [8] Spalart, P. and Allmaras, S., “A One-Equation Turbulence Model for Aerodynamic Flows,” AIAA Paper 92-0439, 1992.
- [9] Frink, N., Parikh, P., and Pirzadeh, S., “A Fast Upwind Solver for the Euler Equations on Three-Dimensional Unstructured Meshes,” AIAA Paper 91-0102, 1991.
- [10] Frink, N., “Upwind Scheme for Solving the Euler Equations on Unstructured Tetrahedral Meshes,” *AIAA Journal*, Vol. 30, 1992, pp. 70–77.
- [11] Frink, N., “Recent Progress Toward a Three-Dimensional Unstructured Navier-Stokes Flow Solver,” AIAA Paper 94-9961, 1994.
- [12] Frink, N., “Tetrahedral Unstructured Navier-Stokes Method for Turbulent Flows,” *AIAA Journal*, Vol. 36, No. 11, 1998, pp. 1975–1982.

- [13] Kwon, O. and Hah, C., "Solution of the 3-D Navier Stokes Equations with a Two-Equation Turbulence Model on Unstructured Meshes Applied to Turbomachinery," AIAA Paper 94-1833, 1994.
- [14] Sarkar, S., Erlebacher, G., Hussaini, M., and Kreiss, H., "The Analysis and Modeling of Dilatational Terms in Compressible Turbulence," *J. Fluid Mech.*, Vol. 227, 1991, pp. 473–495.
- [15] Wilcox, D., "Progress in Hypersonic Turbulence Modeling," AIAA Paper 92-0439, 1991.
- [16] Jones, W. and Launder, B., "The Prediction of Laminarization with a Two-Equation Model of Turbulence," *Int. J. Heat Mass Transf.*, Vol. 15, 1972, pp. 301–314.
- [17] Nagano, Y. and Hashida, M., "Improved Form of the  $k$ - $\varepsilon$  Model for Wall Turbulent Shear Flow," *J. Fluid Mech.*, Vol. 109, 1987, pp. 156–160.
- [18] Speziale, C., Abi, R., and Anderson, E., "A Critical Evaluation of Two-Equation Models for Near-Wall Turbulence," AIAA Paper 90-1481, 1990.
- [19] Carlson, J. R., Personal communication, June 1998. Subsonic Aerodynamics Branch, LaRC, Hampton, VA.
- [20] Girimaji, S., "Fully-Explicit and Self-Consistent Algebraic Reynolds Stress Model," NASA CR 198243, 1995.
- [21] Roe, P., "Characteristic Based Schemes for the Euler Equations," *Ann. Rev. Fluid Mech.*, Vol. 18, 1986, pp. 337–365.
- [22] Van Leer, B., "Flux-Vector Splitting for the Euler Equations," *Lecture Notes in Physics*, Vol. 170, 1982, pp. 507–512.
- [23] Abdol-Hamid, K. S., Lashmanan, B., and Carlson, J. R., "Application of Navier-Stokes code PAB3D with  $k$ - $\varepsilon$  Turbulence Models to Attached and Separated Flows," NASA Technical Paper 3480, 1995.
- [24] Pirzadeh, S., "Viscous Unstructured Three-Dimensional Grids by the Advancing-Layers Method," AIAA Paper 94-0417, 1994.
- [25] Spalart, P., "Direct Simulations of Turbulent Boundary Layers up to  $Re_\theta = 1410$ ," *J. Fluid Mech.*, Vol. 187, 1988, pp. 61–98.
- [26] Cook, P., McDonald, M., and Firman, M., "Airfoil RAE 2822-Pressure Distributions and Boundary Layer Wake Measurements," AGARD AR-138, May 1979.
- [27] Rumsey, C. and Vatsa, V., "A Comparison of the Predictive Capabilities of Several Turbulence Models Using Upwind and Central-Difference Computer Codes," AIAA Paper 93-0192, 1993.
- [28] Schmitt, V. and Charpin, F., "Pressure Distributions on the ONERA M6-Wing at Transonic Mach Number," AGARD AR-138, May 1979.



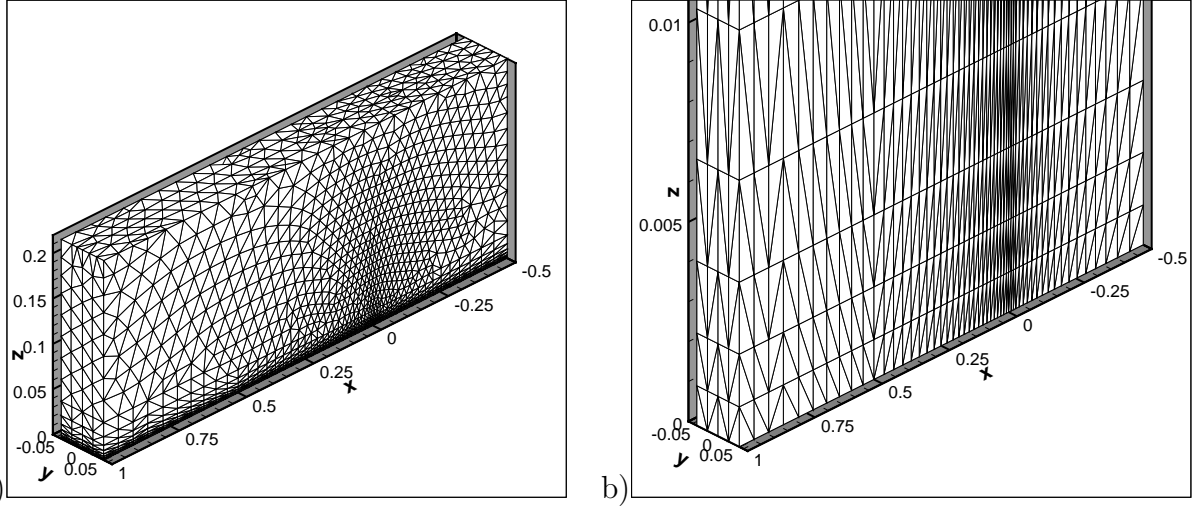


Figure 1: BLT2 grid for a flat plate boundary layer, where the near wall region is unresolved.  
a) whole domain; b) near wall region.

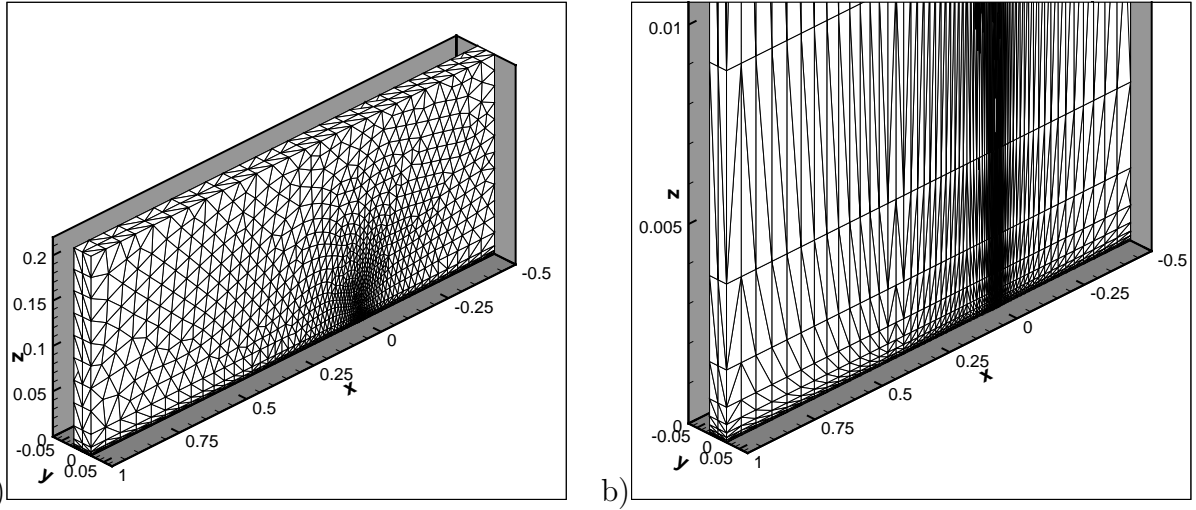


Figure 2: BLT3 grid for a flat plate boundary layer, where the near wall region is resolved.  
a) whole domain; b) near wall region.

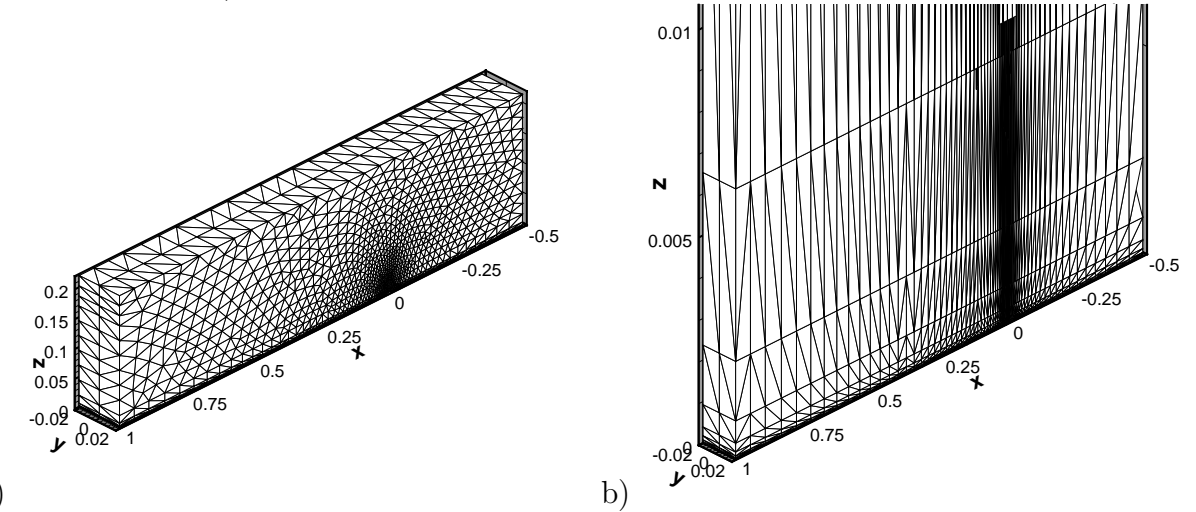


Figure 3: BLT4 grid for a flat plate boundary layer, where the near wall region is resolved.  
a) whole domain; b) near wall region.

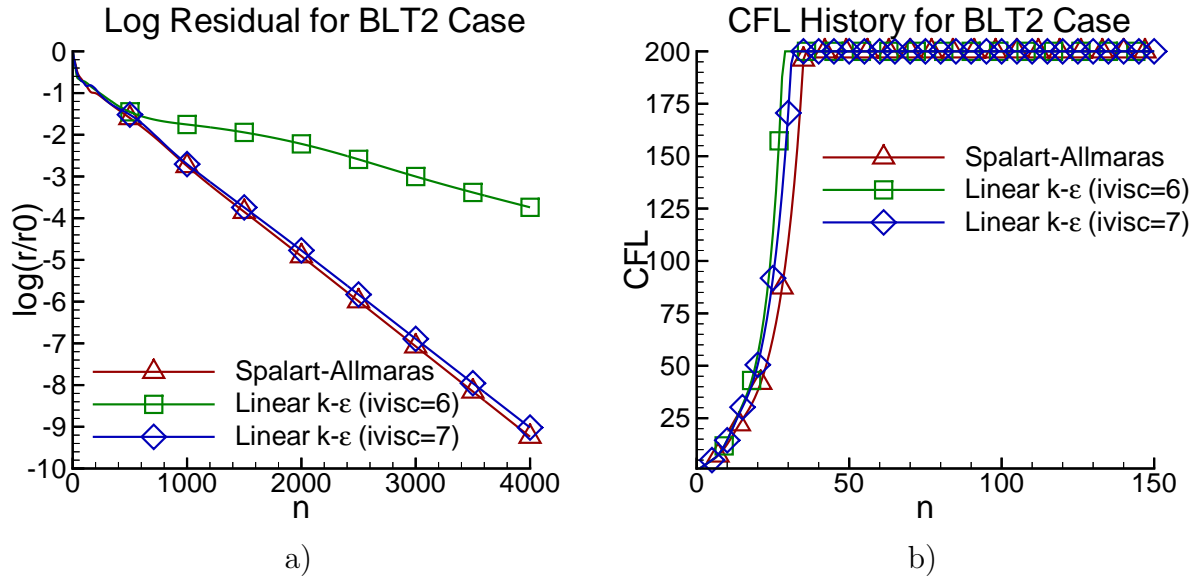


Figure 4: a) Log residual; b) CFL history. BLT2 grid.

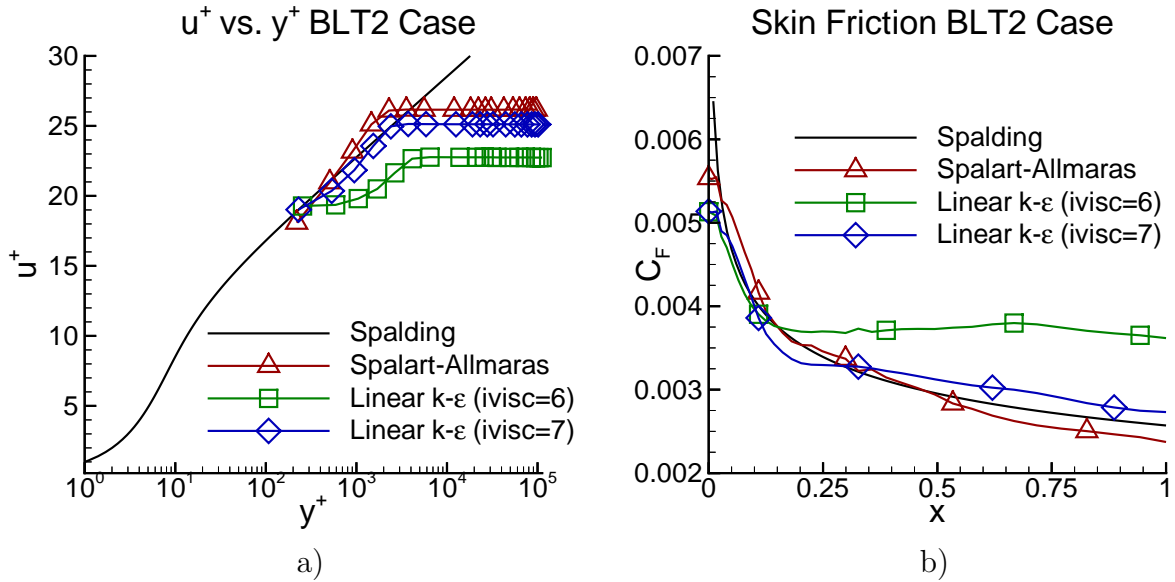


Figure 5: a) Streamwise velocity component in wall coordinates at  $x = 0.5$ ; b) skin friction coefficient. BLT2 grid.

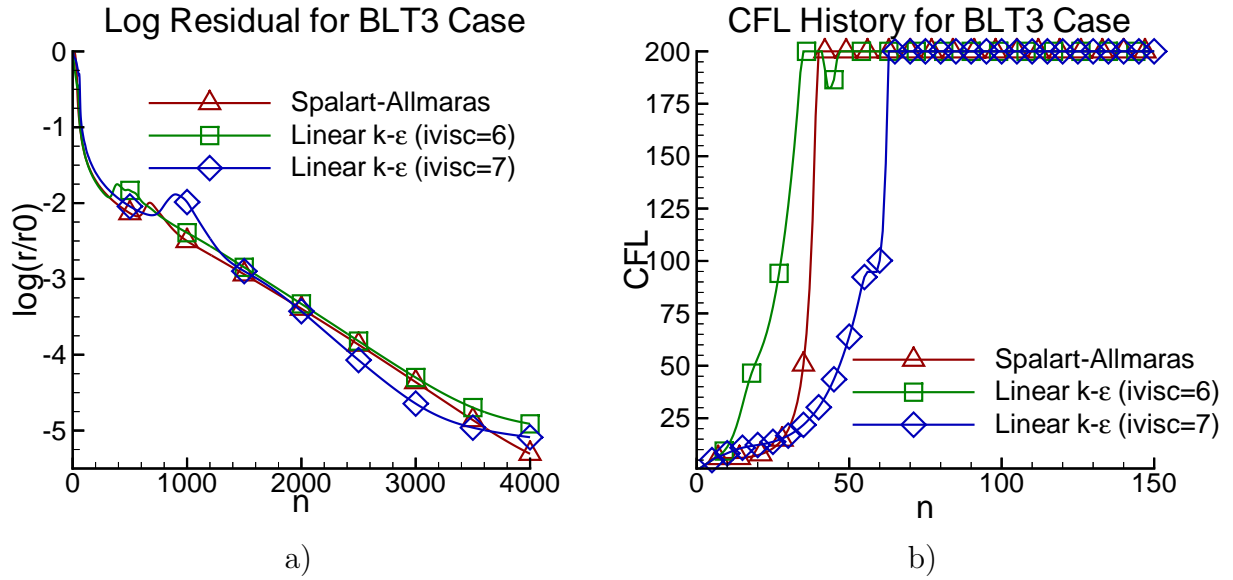


Figure 6: a) Log residual; b) CFL history. BLT3 grid.

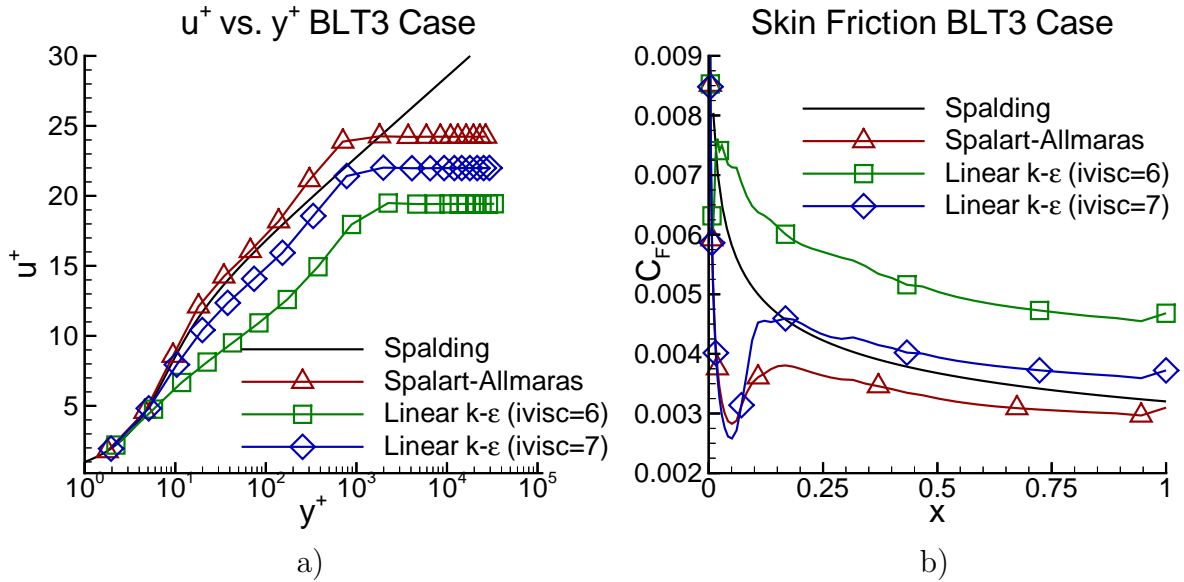


Figure 7: a) Streamwise velocity component in wall coordinates at  $x = 0.5$ ; b) skin friction coefficient. BLT3 grid.

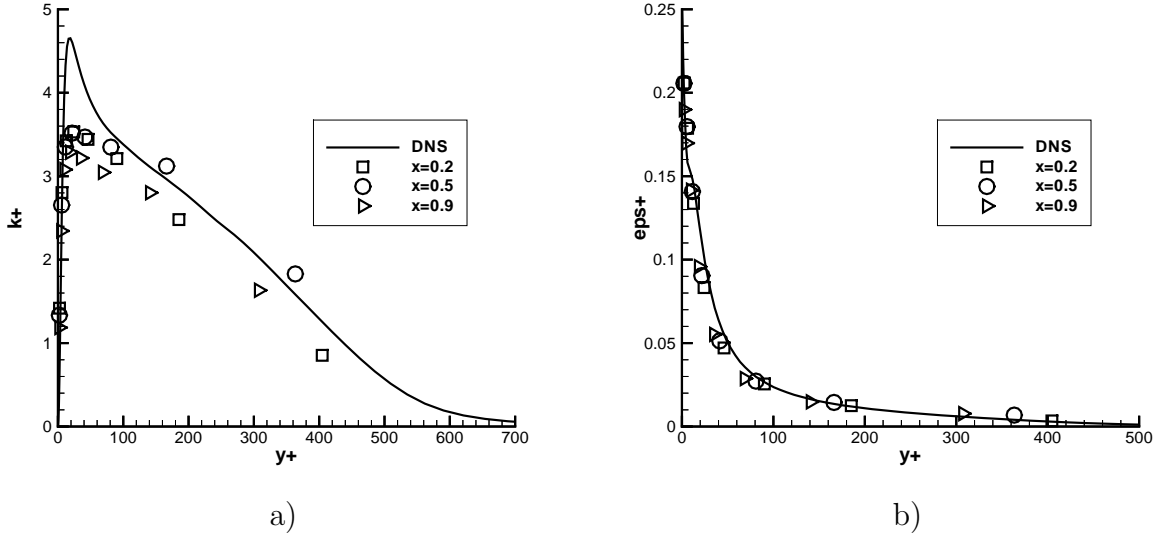


Figure 8: Comparison of turbulent kinetic energy and dissipation rate from the first linear  $k-\varepsilon$  model ( $ivisc=6$ ) with those from the DNS of Spalart [25]. a) turbulent kinetic energy; b) dissipation rate. BLT3 grid.

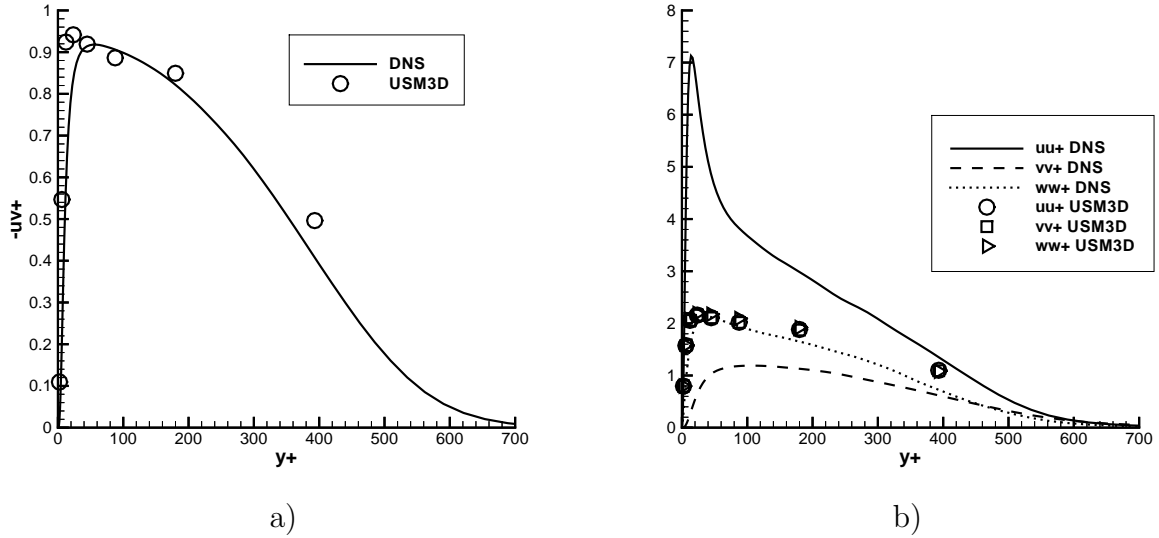


Figure 9: Comparison of Reynolds stress components from the first linear  $k-\varepsilon$  model ( $ivisc=6$ ) at  $x = 0.5$  with those from the DNS of Spalart [25]. a) shear component  $\tau_{12}^T$ ; b) normal components  $\tau_{\alpha\alpha}^T$ . BLT3 grid.

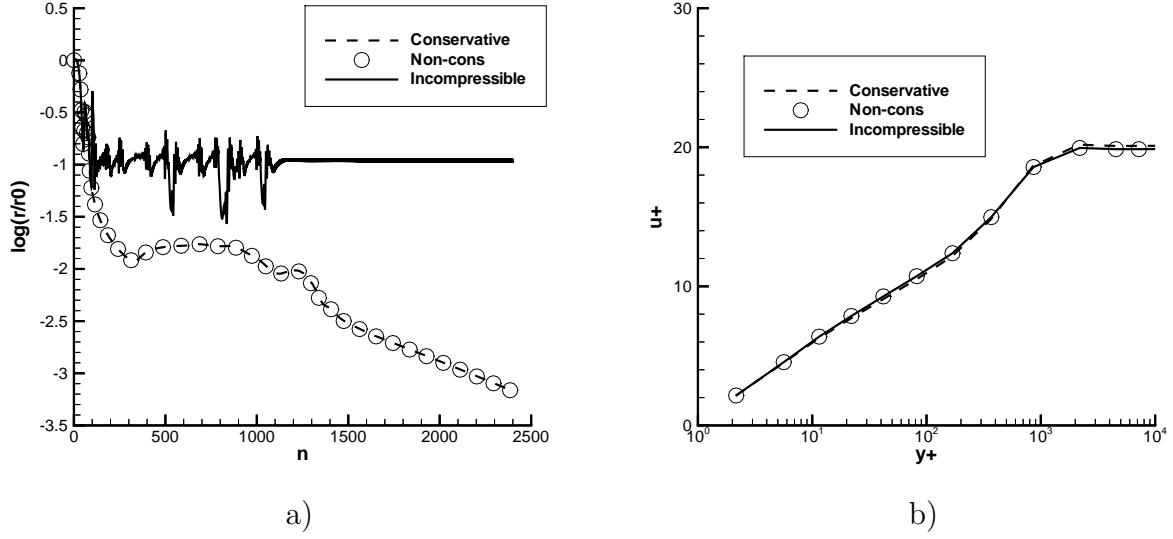


Figure 10: Comparison of solving the  $k$  and  $\varepsilon$  equations in different forms using the first linear model (`ivisc=6`) at  $x = 0.5$ . (a) residual history; (b) velocity component in wall coordinates. BLT3 grid.

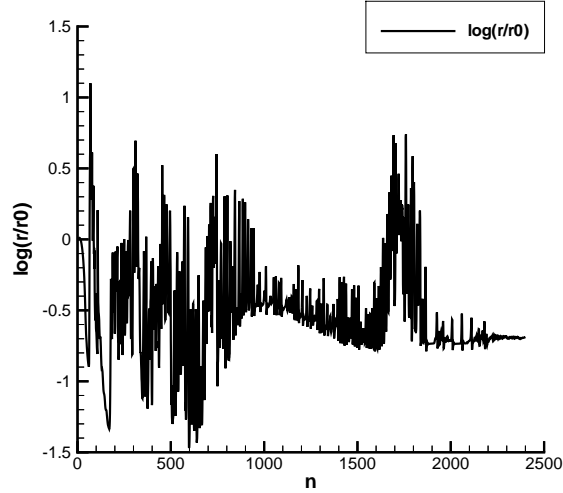


Figure 11: Residual history of the governing equations using the algebraic stress model for the flat plate boundary layer solution on the BLT3 grid.

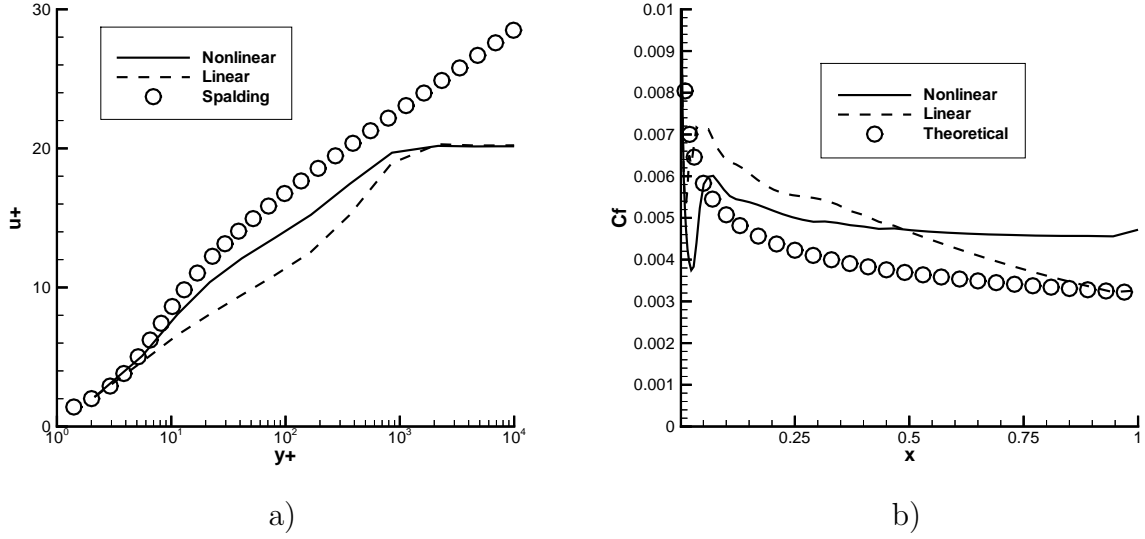


Figure 12: Comparison of a) streamwise velocity component in wall coordinate at  $x = 0.5$  and b) skin friction coefficient using the nonlinear algebraic stress and first linear  $k-\varepsilon$  models for the flat plate boundary layer with the BLT3 grid.

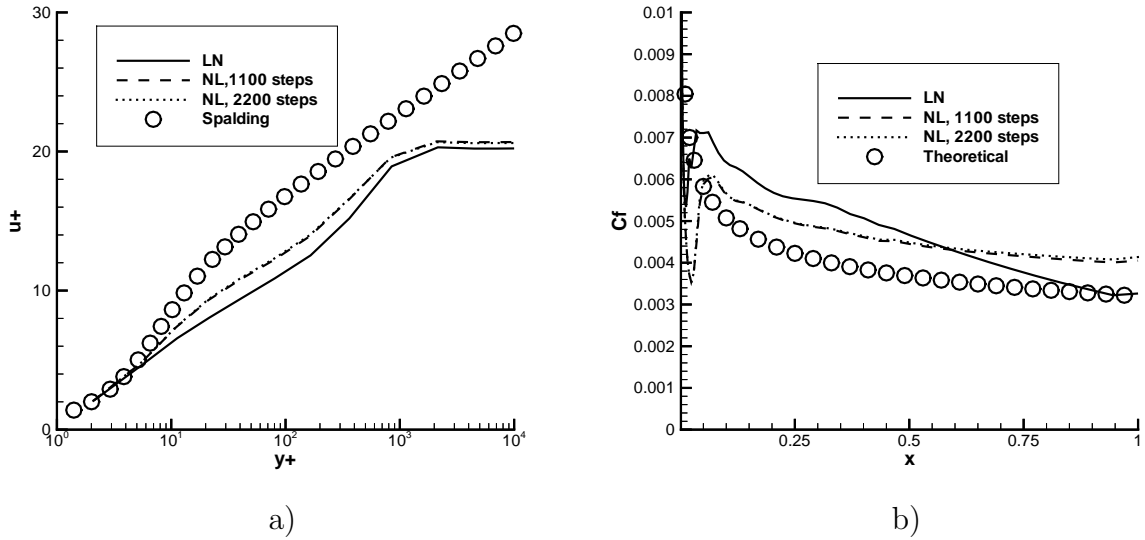


Figure 13: Skin friction coefficient and the streamwise velocity component at  $x = 0.5$  in wall coordinates using the algebraic stress model (NL) restarted from the solution of the first linear  $k-\varepsilon$  model (LN) and run for an additional 1100 and 2200 steps. BLT3 grid.

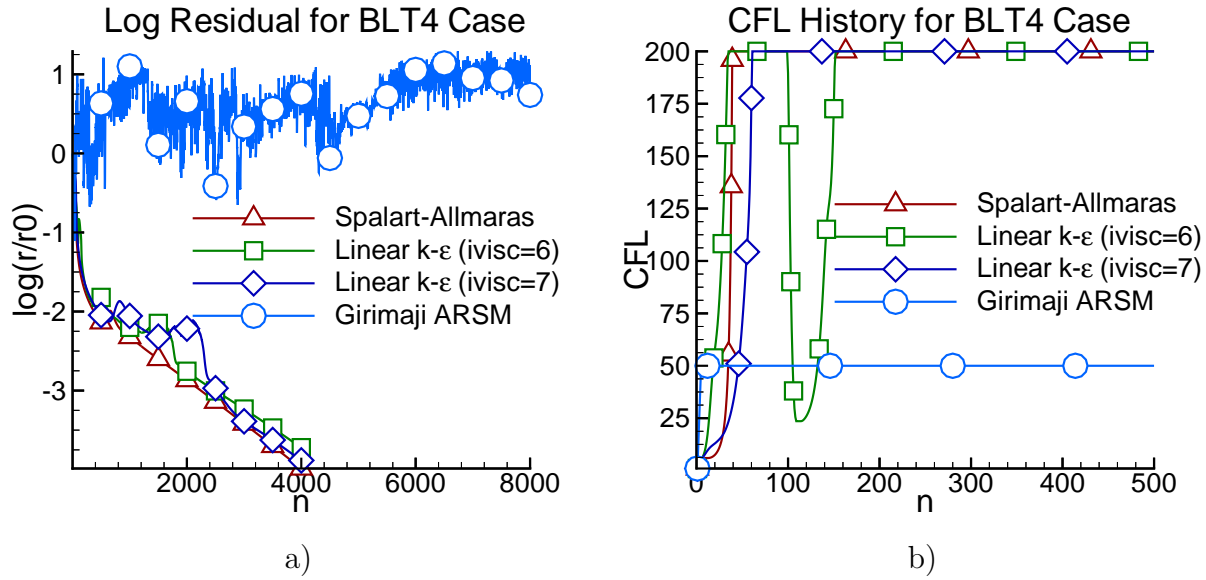


Figure 14: a) Log residual; b) CFL history. BLT4 grid.

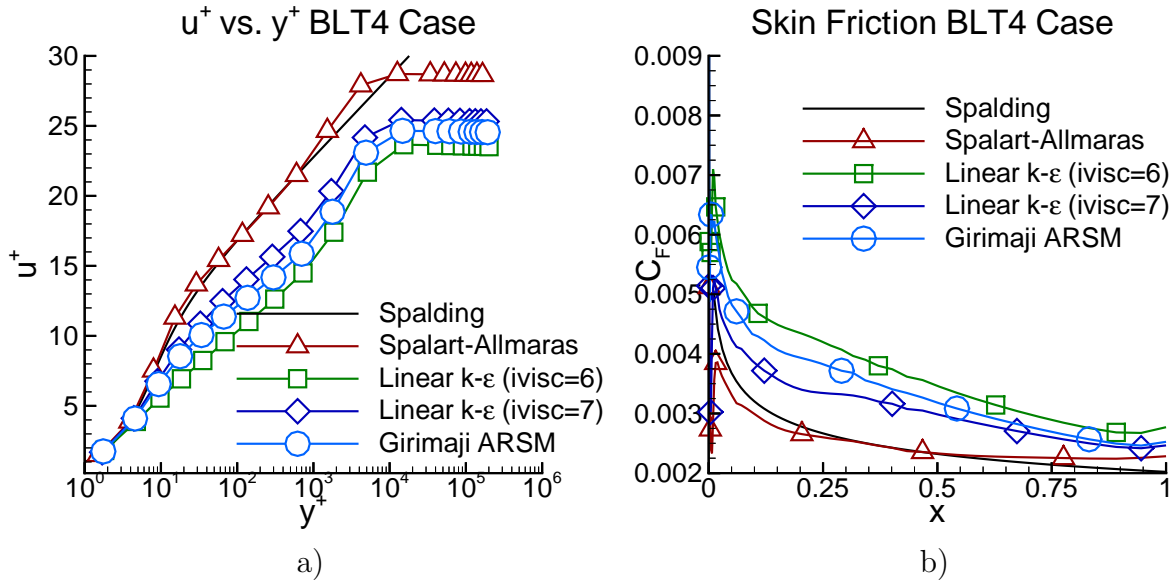


Figure 15: a) Streamwise velocity component in wall coordinates at  $x = 0.5$  and b) skin friction coefficient for BLT4 grid.

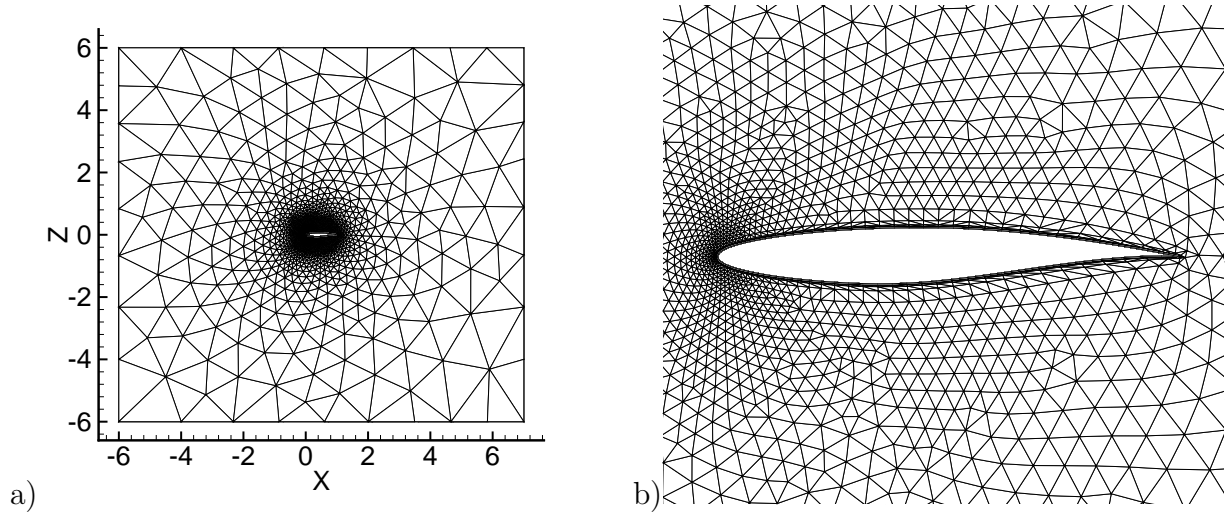


Figure 16: RAE2822 airfoil grid, where the near wall region is resolved. a) whole domain; b) airfoil region.

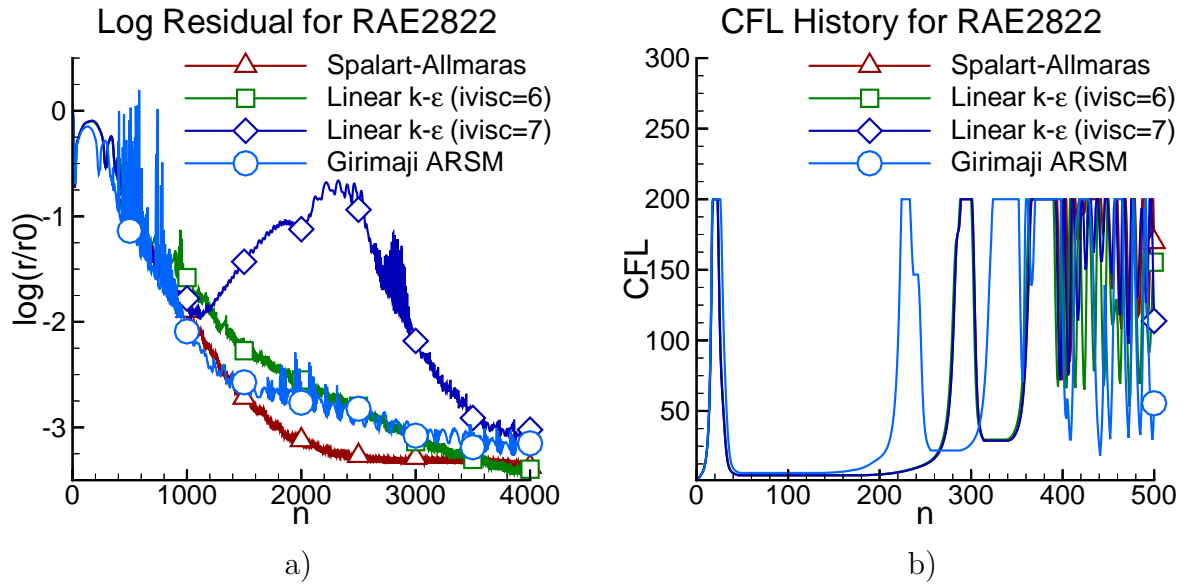


Figure 17: a) Log residual; b) CFL history. RAE2822 airfoil.



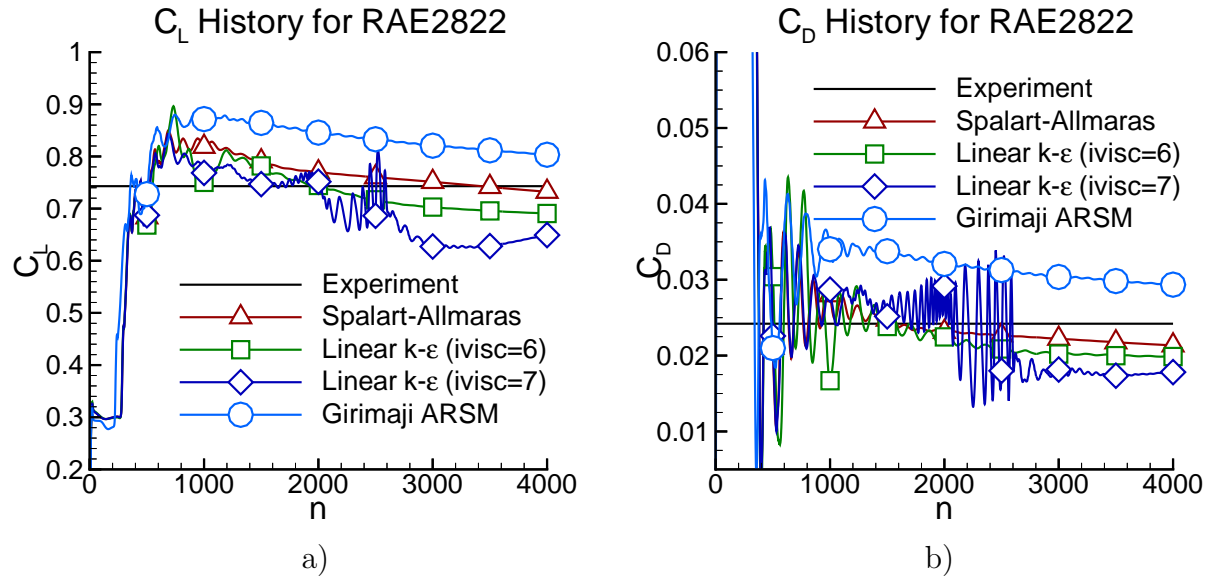


Figure 18: a)  $C_L$ ; b)  $C_D$  history. RAE2822 airfoil.

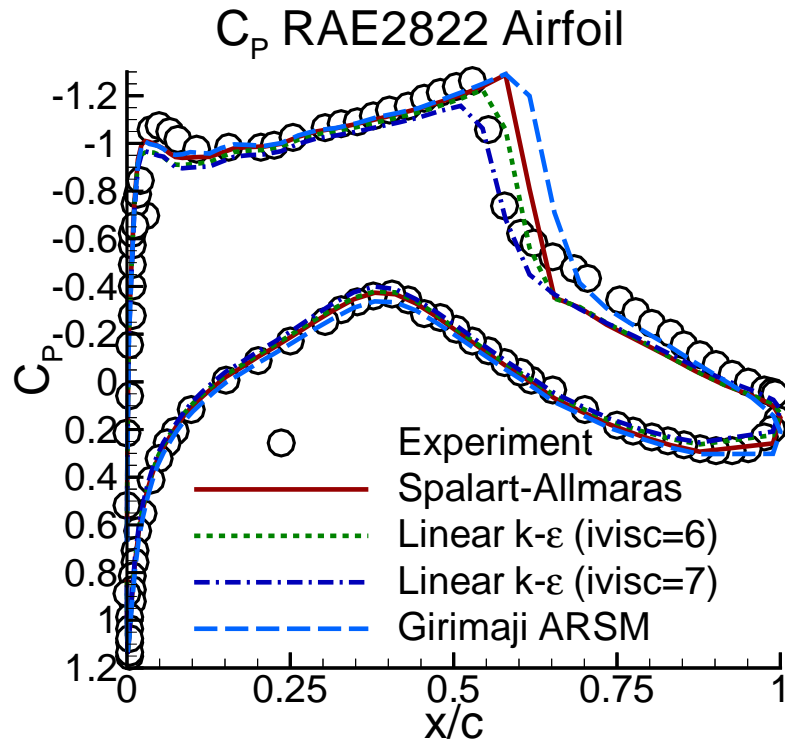


Figure 19: Comparison of coefficient of pressure from each model at  $n = 4,000$  with the experimental data of Cook [26].

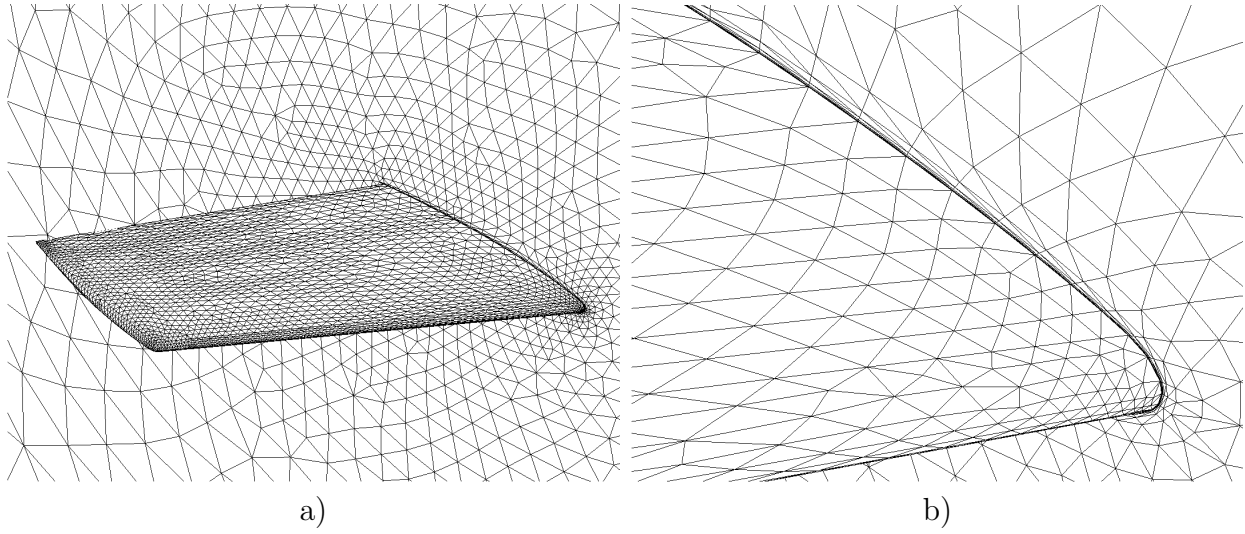


Figure 20: Surface mesh for a) entire wing and b) root region of symmetry plane.

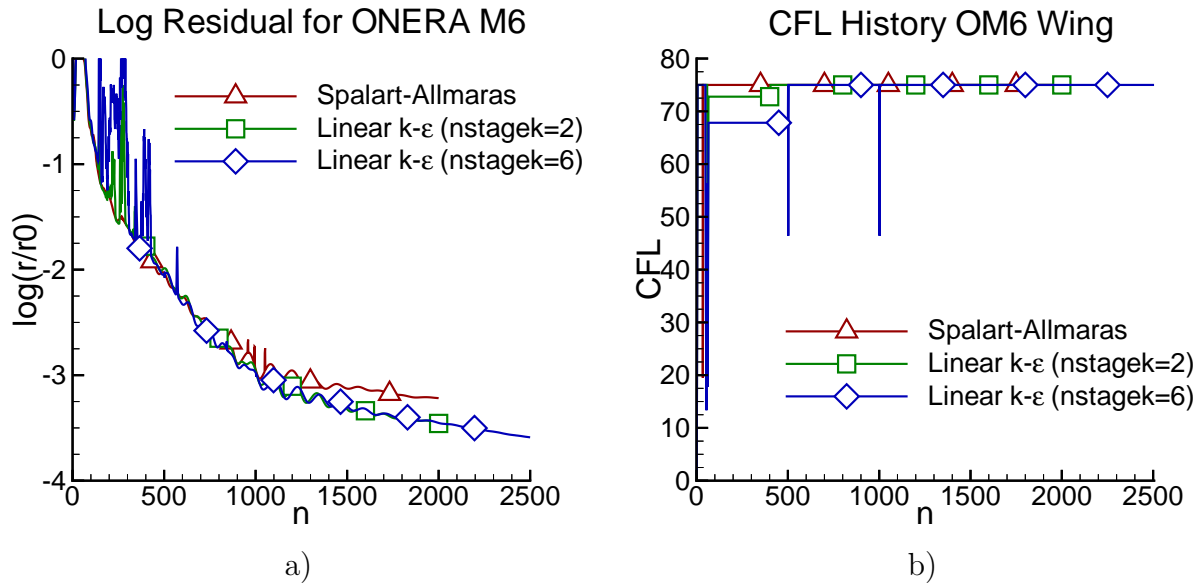


Figure 21: a) Log residual; b) CFL history. ONERA M6 wing case.

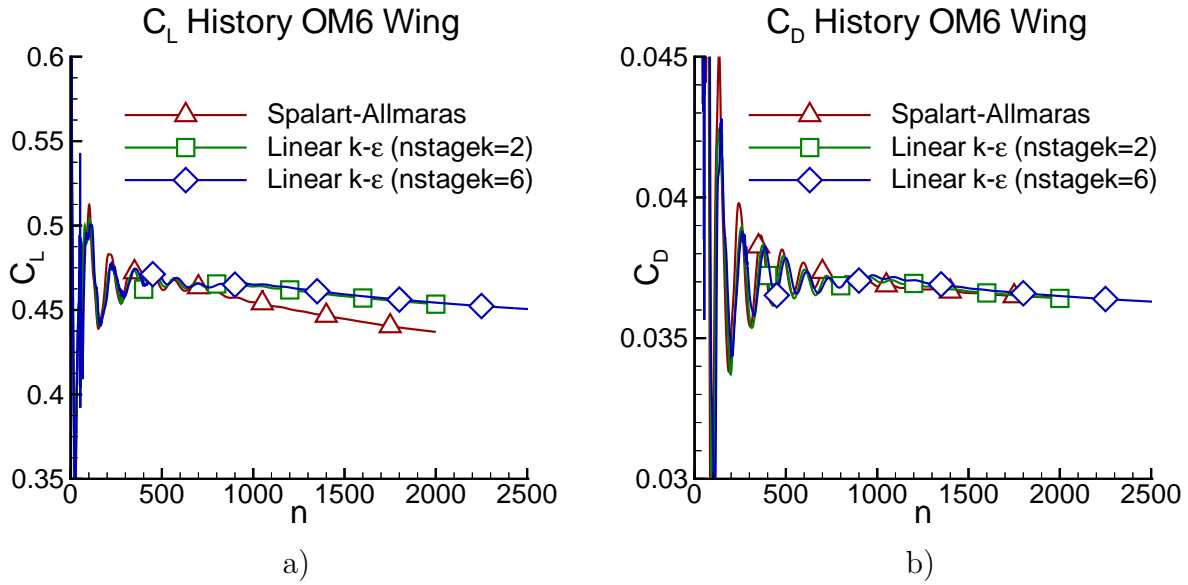


Figure 22: Coefficient of a) lift history; b) drag history. ONERA M6 wing case.

### OM6 USM3Dns Solution – 2000 cycles

$M=0.8447$ ,  $AOA=5.06$ ,  $Re=11.7M$

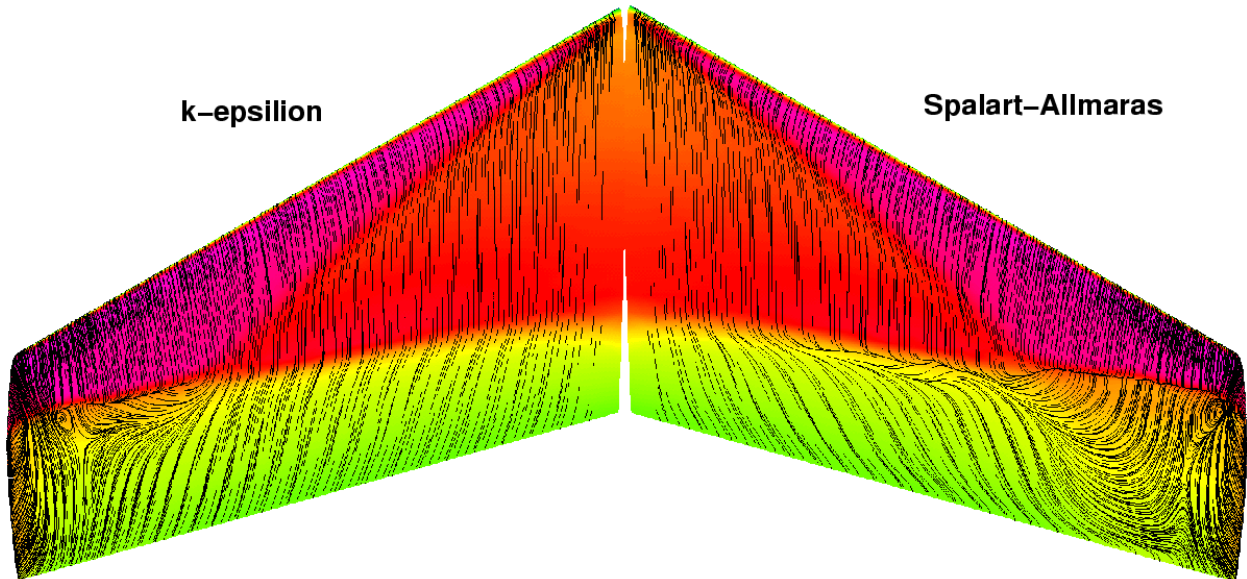


Figure 23: Comparison of  $k-\epsilon$  ( $ivisc=7$ ) and Spalart-Allmaras model computed surface “oil-flow” patterns and flooded pressure contours for the ONERA M6 wing.

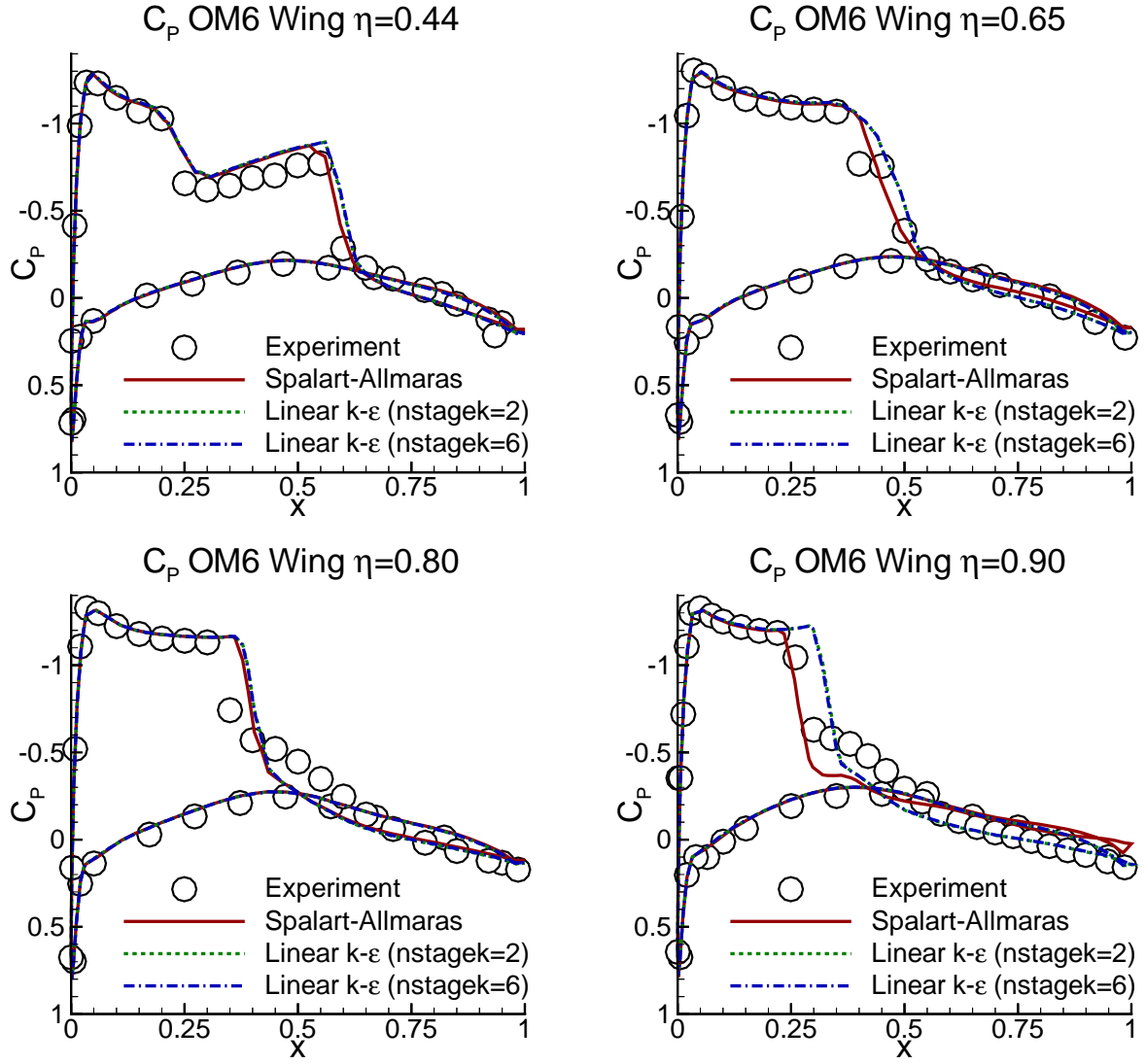


Figure 24: Comparison of coefficient of pressure from each model at  $n = 2,000$  with the experimental data of Schmitt [28].

## A BLT2 Input File

```

USM3D (v5.0+turb) - Flat plate BL Second Linear Model with Wall Function
  Mach      alpha      beta  ReUe,mil  Tinf,dR  itwall  Tw/Tinf ipwall
0.50000  0.00000  0.00000  2.000000  460.0    0      -1.0    0
  sref      cref      bref      xmc      ymc      zmc
1.00000  1.00000  1.0000  0.00000  0.00000  0.00000
  impl      dt/cfl1    iramp      cfl2      cflmin    nstage  iautocfl
  1      -1.00      4      200.    10.00    5      1
  irest      mstage    iresmth    dqmax      ptol    frac_hit  limiter
  0      3      1      0.25    .001    1.0000    0.
nupdate      nwrest    ipltqn      ifast  idiagnos
  10      50      1      0      1
iorder      lapl-avg  high-bc      ifds      ivisc      ckv
  2      1      1      1      7      0.25
  ncyc  nengines      bcfile  compF&M  cldes  idim
  4000      0      1      0      0.    1
Files: 1) Connectivity/grid, 2) Face/b.c., 3) Restart, 4) Flow output (a40)
blt2.cogsg blt2.iface blt2.urest blt2.flo blt2.mapbc
Begin KE Cont
ilhg ikeord icons dtf itk icomp int ut/ul intb ut/ulb inl iwallf bke dkemax isk
-14      1      0 1.0 2      0 1.e-2 10. 1.e-2 10. 0      1 1. 0.00 0
ratiokp nstagek
0.00      5
End KE Cont

```

## B BLT3 Input File

```

USM3D (v5.0+turb) - Flat plate BL Second Linear Model without Wall Function
  Mach      alpha      beta  ReUe,mil  Tinf,dR  itwall  Tw/Tinf ipwall
0.50000  0.00000  0.00000  2.000000  460.0    0      -1.0    0
  sref      cref      bref      xmc      ymc      zmc
1.00000  1.00000  1.0000  0.00000  0.00000  0.00000
  impl      dt/cfl1    iramp      cfl2      cflmin    nstage  iautocfl
  1      -1.00      4      200.    10.00    5      1
  irest      mstage    iresmth    dqmax      ptol    frac_hit  limiter
  0      3      1      0.25    .001    1.0000    0.
nupdate      nwrest    ipltqn      ifast  idiagnos
  10      50      1      0      1
iorder      lapl-avg  high-bc      ifds      ivisc      ckv
  2      1      1      1      7      0.25
  ncyc  nengines      bcfile  compF&M  cldes  idim
  4000      0      1      0      0.    1
Files: 1) Connectivity/grid, 2) Face/b.c., 3) Restart, 4) Flow output (a40)
blt3.cogsg blt3.iface blt3.urest blt3.flo blt3.mapbc
Begin KE Cont
ilhg ikeord icons dtf itk icomp int ut/ul intb ut/ulb inl iwallf bke dkemax isk
-14      1      0 1.0 2      0 1.e-2 10. 1.e-2 10. 0      0 1. 0.0 0
ratiokp nstagek
0.00      5
End KE Cont

```

## C BLT4 Input File

```

USM3D (v5.0+turb) - Flat plate BL Second Linear Model without Wall Function
  Mach      alpha      beta  ReUe,mil  Tinf,dR  itwall  Tw/Tinf ipwall
0.50000  0.00000  0.00000  20.00000  460.0    0      -1.0    0
  sref      cref      bref      xmc      ymc      zmc
1.00000  1.00000  1.0000  0.00000  0.00000  0.00000
  impl      dt/cfl1    iramp      cfl2      cflmin    nstage  iautocfl
  1      -1.00      4      200.    10.00    5      1
  irest      mstage    iresmth    dqmax      ptol  frac_hit  limiter
  0      3      1      0.25    .001    1.0000    1.
nupdate      nwrest    ipltqn      ifast  idiagnos
  10      50      1      0      1
iorder      lapl-avg  high-bc      ifds      ivisc      ckv
  2      1      1      1      7      0.25
ncyc  nengines  bcfile  compF&M  cldes  idim
4000      0      1      0      0.    1
Files: 1) Connectivity/grid, 2) Face/b.c., 3) Restart, 4) Flow output (a40)
blt4.cogsg blt4.iface blt4.urest blt4.flo blt4.mapbc
Begin KE Cont
ilhg ikeord icons dtf itk icomp int ut/ul intb ut/ulb inl iwallf bke dkemax isk
-14  1  0 1.0  2  0 1.e-2 10. 1.e-2 10. 0  0 1.0  0.00  0
ratiokp nstagek
0.00  5
End KE Cont

```

## D RAE2822 Input File

```

USM3D (v5.0+turb) - RAE2822 Airfoil Second Linear Model without Wall Function
  Mach      alpha      beta  ReUe,mil  Tinf,dR  itwall  Tw/Tinf ipwall
0.75000  2.81000  0.00000  6.200000  460.0    0      -1.0    0
  sref      cref      bref      xmc      ymc      zmc
0.20000  1.00000  0.2000  0.00000  0.00000  0.00000
  impl      dt/cfl1    iramp      cfl2      cflmin    nstage  iautocfl
  1      -1.00      4      200.    10.00    5      1
  irest      mstage    iresmth    dqmax      ptol  frac_hit  limiter
  0      3      1      0.25    .001    1.0000    0.
nupdate      nwrest    ipltqn      ifast  idiagnos
  10      50      1      0      1
iorder      lapl-avg  high-bc      ifds      ivisc      ckv
  2      1      1      1      7      0.25
ncyc  nengines  bcfile  compF&M  cldes  idim
4000      0      1      0      0.    1
Files: 1) Connectivity/grid, 2) Face/b.c., 3) Restart, 4) Flow output (a40)
rae3.cogsg rae3.iface rae3.urest rae3.flo rae3.mapbc
Begin KE Cont
ilhg ikeord icons dtf itk icomp int ut/ul intb ut/ulb inl iwallf bke dkemax isk
-14  1  0 1.0  2  0 1.e-2 1.0 1.e-2 1.0 0  0 1.0  0.25  0
ratiokp nstagek
0.05  5
End KE Cont

```

## E ONERA M6 Wing Input File

USM3D (v5+turb) - ONERA M6 wing

Mach	alpha	beta	ReUe,mil	Tinf,dR	itwall	Tw/Tinf	ipwall
0.84470	5.06000	0.00000	21.191770	460.0	1	-1.0	0
sref	cref	bref	xmc	ymc	zmc		
0.52550	0.66700	1.00000	0.00000	0.00000	0.00000		
impl	dt/cfl1	iramp	cfl2	cflmin	nstage	autocfl	
1	-75.0000	1	75.	10.0	6	0	
irest	mstage	iresmth	dgmax	ptol	frac_hit	limiter	
1	3	1	0.25	0.001	0.001	0.	
nupdate	nwrest	ipltqn	ifast	idiagnos	nodeypl		
10	100	2	0	2	0		
iorder	lapl-avg	high-bc	ifds	ivisc	ckv		
2	1	1	1	7	0.25		
ncyc	nengines	bcfile	compF&M	cldes	idim		
500	0	1	0	0.	1		

Files: 1) Connectivity/grid, 2) Face/b.c., 3) Restart, 4) Flow output (a40)

om6ke\_c.cogsg

om6ke\_c.iface

om6ke\_c.urest

om6ke\_c.flo

om6ke\_c.mapbc

Begin KE Cont

ilhq	ikeord	icons	dtf	itk	icomp	int	ut/ul	intb	ut/ulb	inl	iwallf	bke	dkemax	isk
------	--------	-------	-----	-----	-------	-----	-------	------	--------	-----	--------	-----	--------	-----

-14	1	0	1.	2	0	1.e-2	10.	1.e-2	10.	0	0	1.	0.25	0
-----	---	---	----	---	---	-------	-----	-------	-----	---	---	----	------	---

ratiokp nstagek

0.10	6
------	---

End KE Cont

<b>REPORT DOCUMENTATION PAGE</b>			Form Approved OMB No. 0704-0188	
Public reporting burden for this collection of information is estimated to average 1 hour per response, including the time for reviewing instructions, searching existing data sources, gathering and maintaining the data needed, and completing and reviewing the collection of information. Send comments regarding this burden estimate or any other aspect of this collection of information, including suggestions for reducing this burden, to Washington Headquarters Services, Directorate for Information Operations and Reports, 1215 Jefferson Davis Highway, Suite 1204, Arlington, VA 22202-4302, and to the Office of Management and Budget, Paperwork Reduction Project (0704-0188), Washington, DC 20503.				
<b>1. AGENCY USE ONLY</b> (Leave blank)		<b>2. REPORT DATE</b> April 2000		<b>3. REPORT TYPE AND DATES COVERED</b> Contractor Report
<b>4. TITLE AND SUBTITLE</b> Implementation of Advanced Two Equation Turbulence Models in the USM3D Unstructured Flow Solver			<b>5. FUNDING NUMBERS</b>  WU 522-31-21-01  NAS4-50066	
<b>6. AUTHOR(S)</b> Qunzhen Wang, Steven J. Massey, and Khaled S. Abdol-Hamid				
<b>7. PERFORMING ORGANIZATION NAME(S) AND ADDRESS(ES)</b> Analytical Services & Materials, Inc. Lancaster, California			<b>8. PERFORMING ORGANIZATION REPORT NUMBER</b>	
<b>9. SPONSORING/MONITORING AGENCY NAME(S) AND ADDRESS(ES)</b>  National Aeronautics and Space Administration Langley Research Center Hampton, VA 23681-2199			<b>10. SPONSORING/MONITORING AGENCY REPORT NUMBER</b>  NASA/CR-2000-210102	
<b>11. SUPPLEMENTARY NOTES</b> Langley Technical Monitor: Neal T. Frink				
<b>12a. DISTRIBUTION/AVAILABILITY STATEMENT</b> Unclassified-Unlimited Subject Category 02                      Distribution: Standard Availability: NASA CASI (301) 621-0390			<b>12b. DISTRIBUTION CODE</b>	
<b>13. ABSTRACT</b> (Maximum 200 words) USM3D is a widely-used unstructured flow solver for simulating inviscid and viscous flows over complex geometries. The current version (version 5.0) of USM3D, however, does not have advanced turbulence models to accurately simulate complicated flow. We have implemented two modified versions of the original Jones and Launder k-epsilon "two-equation" turbulence model and the Girimaji algebraic Reynolds stress model in USM3D. Tests have been conducted for three flat plate boundary layer cases, a RAE2822 airfoil and an ONERA M6 wing. The results are compared with those from direct numerical simulation, empirical formulae, theoretical results, and the existing Spalart-Allmaras one-equation model.				
<b>14. SUBJECT TERMS</b> unstructured, tetrahedral, Navier-Stokes, turbulence model			<b>15. NUMBER OF PAGES</b> 36	
			<b>16. PRICE CODE</b> A03	
<b>17. SECURITY CLASSIFICATION OF REPORT</b> Unclassified	<b>18. SECURITY CLASSIFICATION OF THIS PAGE</b> Unclassified	<b>19. SECURITY CLASSIFICATION OF ABSTRACT</b> Unclassified	<b>20. LIMITATION OF ABSTRACT</b> UL	